https://doi.org/10.1016/j.jcsr.2021.107003

Strength predictions of circular hollow section T-joints of steel grade 1100 MPa

Yancheng CAI, Tak-Ming CHAN * and Ben YOUNG

Department of Civil and Environmental Engineering, The Hong Kong Polytechnic University, Hong Kong

Abstract

This paper presents experimental and numerical investigations of cold-formed high strength steel (CFHSS) circular hollow section (CHS) T-joints. The CFHSS CHS members have nominal 0.2% proof stress of 1100 MPa. The geometric parameters of the T-joints were designed by varying the ratios of β, 2γ and τ. A total of twelve T-joint tests were conducted by applying axial compressive load through the braces without preloading in chords. Non-linear finite element (FE) model was then developed for the CFHSS CHS T-joints. After successful validation, parametric studies were performed by using the verified FE model. The chord plastification failure of the T-joints was mainly found in both test and numerical studies. The relationship between the joint strengths and the variation of geometric ratios were investigated. The test and numerical strengths of the T-joints were used to assess the strength predictions by design equations provided in CIDECT, EN-1993-1-8 and the literature. It was found that these predictions generally provided unconservative predictions. A new equation that considers the effects of geometric ratios on the strengths was proposed based on both the test and numerical results. By adopting the newly proposed equation, the predictions are improved and provide the least scattered results when compared with other predictions.

Key words: Cold-formed high strength steel; chord plastification; circular hollow section; experimental investigation; numerical investigation; tubular T-joints.

* Corresponding author.
E-mail address: tak-ming.chan@polyu.edu.hk

1. Introduction

Steel tubular members with higher strength and higher grade have been developed and produced owing to the advancements in material and fabrication techniques. Nowadays, steel tubular members having yield strength (or 0.2% proof stress, $f_{0.2}$) over 1000 MPa are available in the industry. Dimensions and numbers of members in steel structures can be reduced by using higher strength steel members, thereby reducing the overall weight of the structure with the associated reduction in transportation resources, handling time, erection time and costs of foundation [1]. These advantages are favoured by architects, engineers and developers. However, the current international steel design specifications [2-4] are applicable for structural steel with nominal yield strength (or nominal 0.2% proof stress, $f_{0.2,n}$) up to 700 MPa, for example, the European Code EN 1993-1-12 [2]. This gap in terms of steel grades between the market and design specifications has driven the investigations on high strength steel with nominal yield strength not less than 690 MPa, in the last decade, including investigations on material properties [5-11], beams subjected to three-point bending and/or four-point bending [12-15], columns subjected to axial compression and/or combined axial compression and bending [16-25] as well as bolted connections [26-33] and welded joints [34-42]. Furthermore, the high strength steel tubular members were also investigated in composite structures, such as concrete-filled steel columns with circular hollow section (CHS) [43] as well as square and rectangular hollow sections [44]. These research works have led to the newly proposed design rules that are currently not covered by the current steel design specifications [2-4], such as design of high strength steel beams subjected to bending [13,15], high strength steel columns under axial compression [18-20] as well as combined compression and bending [22].

Welded joints in steel tubular structures are widely used in onshore and offshore structures. Design guides for tubular welded joints under different loading conditions have been developed based on extensive research projects on steel structures. These research projects were mainly conducted under the

direction of Comité International pour le Développement et l'Etude de la Construction Tubulaire (CIDECT) and International Institute of Welding (IIW) Sub-commission XV-E [45-46]. The IIW published its first edition of design recommendation on static strength of steel tubular joints [47] in 1981, the second edition [48] in 1989 and then the third edition [49] in 2009. At the same period, the CIDECT provided its first edition for the design guides of CHS joints [50] in 1991 and rectangular hollow section (RHS) joints [51] in 1992; and the second edition for CHS joints [52] in 2008 and RHS joints [53] in 2009. These design guidelines [47-53] are applicable for steel tubular joints under predominantly static loading. The design recommendations proposed by IIW and CIDECT have been adopted by many international standards [3,4, 54-56] around the world. These designs are generally valid for both cold-formed and hot-finished steel members with nominal 0.2% proof stress not exceeding 460 MPa and nominal wall thickness ranging from 2.5 mm to 25.0 mm, as summarised by Tong and Zhao [46]. The current emerged higher strength steel tubular members in industry are not covered by these design guidelines. Hence, these design guidelines may not cater for the needs in the safe and reliable design of high strength steel tubular joints in steel structures.

In terms of the effects on strength of welded steel tubular joints due to the higher steel grades utilised, the current version (2nd Version) of CIDECT [52,53], as compared to its first edition [50,51] for steel grade up to S355 (having nominal yield strength of 355 MPa), extended the steel grade up to S460 (having nominal yield strength of 460 MPa) by limiting the design yield strength not higher than 0.8 times the ultimate strength (0.8f_u), and imposing a further reduction factor of 0.9 in the design. Likewise, a reduction factor of 0.9 is specified in EN 1993-1-8 [55] to enable the design equations applicable to steel grades exceeding S355 but limited to S460. The EN 1993-1-12 [2] further extends the design to steel grade up to S700 by multiplying another reduction factor of 0.8. These reduction factors are imposed mainly for the consideration of possibly lower rotation and deformation capacity as well as for

the required sufficient ductility [52,53]. However, the suitability of these design rules with reduction factors for higher strength steel tubular joints are controversial [41], for examples, the recent numerical investigations on high strength steel (nominal yield strength up to 1100 MPa) CHS X-joints by Lan *et al.* [38] showed that the strength predictions by CIDECT [52] and EN-1993-1-8 [55] became increasingly unconservative as steel yield strength increased. A new design equation was proposed by Cai *et al.* [57] for high strength steel ($f_{0.2}$ up to 1100 MPa) CHS X-joints with braces subjected to axial loading and failure of chord plastification (chord face failure). It is shown that the proposed equation provides more accurate and less scattered strength predictions than those predicted by the CIDECT [52], EN-1993-1-8 [55] and Lan *et al.* [38].

Design rules for welded circular tubular (both brace and chord members) joints failed by chord plastification are, in principle, based on the analytical model firstly proposed by Togo [58]. The proposed model indicates that the chord plastification strength of the joints subjected to axial loading in braces is the function of the yield strength together with the square of chord wall thickness (t_0). Based on this principle, design equations for circular tubular joints were developed by carrying out extensive experimental and numerical investigations, where the key geometric parameters were considered in the equations, including the ratios of brace outer diameter (d_1) to chord outer diameter (d_0) in $\beta = d_1/d_0$, the d_0 to t_0 ratio in $2\gamma = d_0/t_0$ as well as brace wall thickness (t_1) to the t_0 in $\tau = t_1/t_0$. With the shortcomings of the current design guidelines as discussed earlier and the tubular joints associated with the rapid development in high strength steel members, the purposes of this study are to investigate the effects of the key geometric parameters on the chord plastification strengths of cold-formed high strength steel (CFHSS) CHS T-joints by experimental testing and numerical modelling; and to assess the applicability of the existing design guidelines for the T-joints with nominal 0.2% proof stress of 1100 MPa. The CFHSS T-joints are loaded by axial compressive force in braces without chord preloading. Finally, a

new design equation is derived for the strength prediction of CFHSS CHS T-joints failed by chord plastification.

2. Experimental investigation

2.1 *Design of test specimens*

A series of CFHSS CHS T-joint (see Figure 1) tests were conducted in this study. The CFHSS members had the nominal 0.2% proof stress ($f_{0.2,n}$) of 1100 MPa, and four different sections ($D \times t$ in millimetre) with the nominal outer diameter (D) and thickness (t) of 89×4, 108×4, 133×4 and 139×6. The sections of 89×4, 108×4, 133×4 and 139×6 were used as the chord members of the T-joints. The nominal section size that had outer diameter smaller than or equal to that of the chord member was paired as the brace member. Hence, in the design of test specimens, the geometric parameters that are related to the resistance of CHS T-joints were considered, namely, the ratios of β ($\beta = d_1/d_0$), 2γ ($2\gamma = d_0/t_0$) and τ ($\tau = t_1/t_0$). The specimens are generally identified by two segments, namely, segment of the brace section followed by that of the chord section (brace – chord), as shown in Table 1. If it was a repeated test specimen, it was indicated by -r in the labelling.

In this investigation, the chord length (l_0) of the T-joints was determined by d_1+3d_0+180 mm. The length of steel sitting at each chord end was 90 mm (see the schematic view of test setup in Figure 2). The design principle of l_0 was based on the fact that adequate load distribution in the chord member was achieved and the stresses at the brace and chord intersection were not affected by the chord ends, as illustrated in the numerical analysis in this study. The chord length of the T-joint specimens in this study satisfied the minimum member length ($d_1 + 3d_0$) for the Interior-One-Flange (IOF) loading case of web crippling tests specified in NAS [60]. The nominal brace length (l_1), from the top (crown toe) of the chord to the end of the brace, was generally taken as $2d_1$ (except for specimens 133×4–139×6, 139×6–139×6 and 133×4–133×4) so as to avoid global buckling of the brace member and possible interaction

of stresses between the brace ends.

In all the CFHSS CHS T-joint specimens, the chord member was oriented such that the weld seam of the section was at 90 degrees away from the top of the chord (see Figure 1(a)). The weld seam of the brace member was oriented at 90 degrees from the longitudinal direction of the chord member. The brace member was wire-cut at both ends with one end flat and another end fitting the profile of the paired chord [61]. The dimensions of each CFHSS CHS T-joint specimen were measured and the average values for each dimension are tabulated in Table 1. The geometric ratios of β, τ and 2γ were calculated from the measurements. In summary, the β, τ and 2γ of the test specimens varied from 0.65 to 1.02, from 0.66 to 1.01 and from 22.72 to 34.32, respectively. It should be noted that the measured dimensions may be slightly larger than the nominal dimensions, however, the differences are not significant.

2.2 *Welding and material properties*

A robotic gas metal arc welding (GMAW) was employed in the welding between brace and chord of the CFHSS CHS T-joints, which is the same as those for CFHSS tubular joints [40,42,57]. The AWS D1.1M Specification [62] was followed in the fabrication of the T-joints. A low alloy carbon steel wire with a diameter of 1.2 mm was used as a filler material. It conformed to Class ER120S-G of the AWS A5.28M Specification [63]. The $f_{0.2,n}$, nominal tensile strength ($f_{u,n}$) and elongation of the steel wire were 930 MPa, 980 MPa and 19%, respectively [40,42]. The sizes of weld legs (see Δ_1 and Δ_2 in Figure 1(b)) in the T-joint specimens are greater than the minimum value specified in the AWS D1.1M Specification [61]. This minimum value is set as the maximum of $1.5t_{min}$ or 3 mm, where t_{min} is the thickness of the thinner tube in the joint. The welding throat thickness (Δ_3) of the specimens was also measured. The average measured values for the welding details of the CHS T-joint specimens are also tabulated in Table 2.

Tensile coupon tests were conducted to obtain the material properties of the CFHSS circular tubes.

141 The coupons were machined from the centre of the face at 90˚ from the seam weld in the CFHSS tubes,
142 which represented the crown location at the chord of the T-joints (see Figure 1(a)). The dimension of the
143 coupon specimens had 4 mm width and 25 mm gauge length. The specimens were tested between two
144 pins through specially designed grips such that tension load was applied through the centroid of the
145 coupon [8]. Two strain gauges were used to measure the initial Young's modulus of the material, while
146 an extensometer was used to obtain the rest of the stress-strain curve until fracture. The material
147 properties that based on the 25 mm gauge length of the coupon specimen were obtained, including the
148 modulus of elasticity (E), the measured static 0.01% proof stress ($f_{0.01}$), $f_{0.2}$ and tensile strength (f_u), strain
149 at tensile strength (ε_u) and fracture failure (ε_f), as shown in Table 3. The Ramberg-Osgood parameter (n)
150 was calculated according to $n = ln(0.2/0.01)/\ln(f_{0.2}/f_{0.01})$. Figure 3 illustrates the stress-strain curves
151 obtained from the coupon tests.

152 2.3 *Test rig and* procedure

153 The CFHSS CHS T-joints were tested in a servo-controlled hydraulic testing machine. The photo of
154 test setup for specimen 89×4 - 89×4 is shown in Figure 4. The chord ends of the T-joints were positioned
155 in a set of special steel sittings (see Figures 2 and 4) that match the outer surface of the half sections.
156 The steel sittings were fastened to steel bearing plates that supported by the rollers in order to provide a
157 pure flexural boundary condition for the chord member. The roller at each chord end was rested on a
158 solid rigid support which in turn was securely fastened onto the actuator ram of the testing machine. A
159 special ball bearing was used at the top of the testing machine. The ball bearing can be self-adjusted
160 according to the flat profile of the top brace end such that a uniformly distributed load can be applied to
161 the brace of the specimen.

162 The T-joint specimen was carefully positioned by levelling and alignment during the test setup [61].
163 The specimen was rested on the rollers through the special steel sittings where the rollers were

temporarily held in position using magnetic strips. Initially, the special ball bearing was unlocked and can rotate in any direction. The actuator ram of the testing machine was then slowly moved up to a preload value of 2.0 to 4.0 kN. This preload process facilitates the self-adjustment of the special ball bearing according to the flat brace end, and eliminates any gaps between the specimen, steel sittings and rollers. After preloading, the position of the ball bearing was then locked from any major and minor axis rotations for the rest of the test. In order to allow free translation movement of the rollers during the test, the magnetic strips were then removed after securely preloading the T-joint specimen. For safety purpose, the rollers were attached with metallic chains to the solid rigid supports in order to prevent them flying off during the test.

The local deformations at the joint region were carefully recorded with the help of calibrated linear variable displacement transducers (LVDTs). The chord face indentations were measured at the chord crown in each side of the brace with the help of extension arms attached to the tips of the respective LVDTs (e.g., LVDT 1 as shown in Figure 2). In this study, the chord indentation was measured along the direction of the brace (axial loading direction) adjacent to the weld toe at the crown of chord for all the specimens. The deflection due to bending of the chord member was measured through a pair of LVDTs (e.g., LVDTs 5&6 as shown in Figure 2) which were positioned at the mid-span of the chord in a symmetric manner. An aluminium bar with a profile matching the outer surface of the chord was carefully glued at the bottom of the chord. Hence, the deflection of the chord at the mid-span due to bending was detected by the average reading of the LVDTs (i.e., LVDTs 5&6 as shown in Figure 2) through the aluminium bar. The chord indentation (u) of the T-joints was obtained by the average readings of the LVDTs 1&2 subtracting the average readings of the LVDTs 5&6. Furthermore, two horizontal LVDTs (e.g., LVDTs 2&4 as shown in Figure 2) with Poly Methyl Methacrylate (PMMA) plates connected to their tips were used to measure chord horizontal deflections (v) at the mid-span of

187 the chord. The use of PMMA plates connected to the tips of these LVDTs ensured that the measured
188 deformations were unaffected by overall vertical displacements of the chord during loading, as well as
189 the maximum chord horizontal deformations could be captured irrespective of their occurrence at the
190 junction region of the T-joint. In addition, the overall axial displacement of the actuator ram was
191 measured through the readings of the vertical LVDT 7, as shown in Figure 4.

192 After preloading, the tests were then conducted by driving the actuator ram in displacement control
193 with a constant loading rate of 0.3 mm/min. The use of displacement control allowed the tests to be
194 continued in the post-peak range. The tests were generally paused for 90 seconds at two locations during
195 the tests, namely near the ultimate loads and at post ultimate loads. The static drops were obtained from
196 the pauses. Hence, the effects of loading rates could be isolated from the test strengths. The tests did not
197 stop until a clear drop of loading was observed. The applied load from the machine and the readings
198 from the LVDTs were recorded by a data acquisition system regularly during the tests.

199 2.4 *Test results*

200 The test results of the CFHSS CHS T-joints are summarized in Table 4. The test strengths were
201 determined from the static load-deformation curves. The static load-deformation curves were obtained
202 from the static drops as mentioned earlier. All the specimens experienced a clear ultimate load (peak
203 load) in the load-deformation curves and failed by chord plastification (chord face failure). The ultimate
204 load (P_u) and the corresponding chord indentation (μ_u) are tabulated in Table 4. In addition, the load
205 ($P_{3\%}$) corresponding to the chord indentation of $\mu_{0.03}$ ($\mu_{0.03} = 0.03d_0$) was also obtained from the test curve
206 and shown in Table 4. Figures 5(a), 6(a), 7(a) and 8(a) illustrate the applied load versus the chord
207 horizontal deformation curves, for specimens with chords of 139×6 mm, 133×4 mm, 108×4 mm and
208 89×4 mm, respectively; while the corresponding load versus the measured chord face indentation curves
209 are shown in Figures 5(b), 6(b), 7(b) and 8(b). The chord deformation of specimen 108×4-133×4 during

test is illustrated in Figure 9(a).

3. Numerical investigation

3.1 *General*

The finite element (FE) model using the ABAQUS program of version 6.20 [64] was developed to simulate the tests of axial loaded CFHSS CHS T-joint specimens. The FEM was validated by the comparisons of strengths, failure modes and load-deformation curves between the numerical results and test results. After successful validation, extensive parametric studies by using the verified FE model were performed.

3.2 *Development of FEM and validation*

The measured specimen dimensions (see Table 1) were used in the development of CHS T-joints in FE model. The shell element type S4R was selected to simulate the brace member and chord member of the CHS T-joints. The previous study by Lan *et al*. [37] showed that the differences are within the deviation of 5%, when comparing the results using S4R element without considering weld detail and those results using solid element type C3D8R with considering weld detail in CHS X-joints. In their analysis, the specimens had the maximum chord diameter of 244.7 mm and thickness of 22.0 mm tested by Puthli *et al*. [35] were used. Hence, in this study, the weld detail of the T-joint specimens was not considered. A more recent study by Lan *et al*. [38] found that the effects of reduced material properties in heat affected zones (HAZ) on the strengths of CFHSS CHS X-joints was relatively insignificant, as the stress in the HAZ could be effectively redistributed to the adjacent areas of base metals. In addition, it was explained that the improved yield strength of steel in CHS X-joints was generally under-utilised due to the adopted indentation limit [38], which will also be illustrated in the load versus chord face indentation curves of the parametric studies in this paper. The effect of steel material properties due to HAZ in the weld region was thus not modelled in the FE model. The finer mesh sizes were adopted in

the weld region with a length of d_0 from the centre line of the joint to the chord end or brace end (see Figure 9(b)); however, coarse elements were used for the rest parts of the joints [37,38,57].

The engineering stress-strain (σ-ε) curves obtained from the coupon tests were converted to true stress (σ_{true}) and logarithmic plastic strain (ε_{true}^{pl}) curves by following Equations (1)-(2):

$$\sigma_{true} = \sigma\,(1 + \varepsilon) \tag{1}$$

$$\varepsilon_{true}^{pl} = ln(1 + \varepsilon) - \frac{\sigma_{true}}{E_s} \tag{2}$$

The converted true stress-true plastic strain curves were assigned to the corresponding braces and chords in the FE model.

The boundary conditions were modelled in accordance with the tests. The applied loads and reactions were transferred between the steel bearing plates and the specimens. The interfaces between the CFHSS sections and the steel bearing plates (solid rigid plates) were modelled using the contact pairs. In each contact pair, one surface is defined as master surface while the other as slave surface. The master surfaces were set in the steel bearing plates, whereas the slave surfaces were set in the CFHSS specimens. The surface-to-surface discretization contact method was employed. It should be noted that the contact surfaces were not allowed to penetrate each other. The surface-to-surface contact with a finite sliding option was used. The "hard contact" was used in the normal direction, whereas in the tangential direction, a coefficient of 0.2 was used to consider the friction penalty contact. The reference point (RP), RP1, was defined at the brace end (see Figure 10). It was fully coupled with the brace end surface. The RP1 was restricted in all degrees of freedom, except for the axial displacement. Proper boundary conditions were assigned to the reference points (RP2 and RP3) of the steel bearing plates to simulate the roller support in the test setup. The RP2 and RP3 were fully coupled with the bottom surfaces of the respective steel bearing plates. The boundary conditions of $U_x = 0$, $U_y = 0$ (U_x and U_y mean the translation along X and Y axes, respectively), $R_y = 0$ and $R_z = 0$ (R_y and R_z mean the rotation about direction in Y and Z axes,

respectively) were assigned to RP2 and RP3 (see Figure 10), to simulate the roller support.

The reference point of RP4 (see Figure 10) was defined in the crown of the chord, with around 6 mm away from the outer surface of the brace. The reference point of RP5 was defined at middle of the chord surface to monitor the horizontal deformation of the T-joint. In addition, the reference point of RP6 was defined at the bottom of the chord at the mid-span. Hence, the chord face indentation of the T-joint could be obtained from the measurements of RP4 and RP6 in Y direction as those measurements in the tests, i.e., ($\left|\Delta_{RP4}\right| - \left|\Delta_{RP6}\right|$). The loads were applied by specifying axial displacements to the RP1 of the FE model, which was identical to the test program by displacement control test method. The geometrical nonlinearity (*NLGEOM) was activated in the FE model to consider the large deformation of the T-joint. Static analysis method was used in performing the FE analysis.

All the specimens from the FE analysis failed by chord plastification, which is the same failure mode as those of the test specimens. The strengths obtained from the FE analysis, namely the strength (P_{FE-1}) corresponding to the value of $\mu_{0.03}$ which obtained from the measurements of RP4 and RP6 in Y direction, and the ultimate strength (P_{FE-u}) are shown in Table 4. The test strengths were compared with the FE analysis strengths by $P_{3\%}/P_{FE-1}$ and P_u/P_{FE-u}. The mean values of $P_{3\%}/P_{FE-1}$ and P_u/P_{FE-u} were 1.05 and 0.96 with the corresponding coefficient of variation (COV) of 0.057 and 0.043. Figure 9(a) illustrates the comparison of failure mode between test and FE analysis for specimen 108×4 - 133×4. The side elevation view of the specimen failure and the stress contour are shown in Figure 9(b). Generally, the higher stresses (reaching yield stress) were found within the length of $1.0d_0$ from the centreline of the joint. Figures 11(a)-(b) further illustrate the comparison of load versus the deformation curves of the CFHSS CHS T-joints between the test and FE results. Overall, it is shown that the developed FE model could replicate the tests of CFHSS CHS T-joints in terms of joint strengths, failure mode and histories of applied load versus deformations.

3.3 *Parametric studies*

After successful validation of the FE model, the FE model was used to perform the parametric studies for the structural performance of CFHSS CHS T-joints subject to axial compression in braces. The geometric parameters of the CHS T-joint design equations [52,55] were considered, and their interactions were reflected in the parameters of the β, τ and 2γ. The length of the braces was taken as $2d_1$ and that of the chords was taken as (d_1 + 180 + $3d_o$). Same as those test specimens, the chord members of the CFHSS CHS T-joints in the parametric studies were not preloaded.

The designed T-joints for the parametric studies are summarized in Table 5. In the joint designs, three different chord members based on the commonly used steel product catalogue were selected to represent the relatively small, medium and large sizes of CHS members, with the dimensions (D×t in millimetre) of 88.9×6.3, 273×12.5 and 508×12.5, respectively. Hence, there are three series of T-joints in terms of chord outer diameter variations (d_o) as represented by Series A, B and C in the content of this paper. In each series, the geometric parameters of the joints were determined based on the predetermined values of β, τ and 2γ. The values of β, τ and 2γ were mainly set as 0.40, 1.00 and 14.11 in Series A. In Series A, the effects of β, τ and 2γ on the joint behaviour were studied by verifying one factor while maintaining the other two factors the same (see Table 5). Hence, the cross-sectional dimensions of the brace and chord members were then determined. By using the same principle, the values of β, τ and 2γ were mainly set as 0.60, 0.60 and 21.84 as well as 0.80, 0.40 and 40.64 for Series B and C, respectively. Same labelling system was adopted as that for the test specimens. Details of the specimens with the geometric ratios are shown in Tables 6-8, for Series A, B and C, respectively.

The material properties of section 108×4 (see Table 3) obtained from the coupon tests were used in the parametric studies. In total, 75 parametric results were generated for the CFHSS CHS T-joints subjected to axial loading in braces. All these 75 T-joints mainly failed by chord plastification. In each

series, the curves of load versus the chord side wall deformation and those of load versus the chord face indentation are plotted, as shown in Figures 12-14 for specimens in Series A, and in Figures 15-17 for Series B and Figures 18-20 for Series C. The chord face indentation (μ) was obtained by the difference in axial displacements of RP4 and RP6 as mentioned earlier. In the figure of each series, the value of chord face indentation equal to 3%d_0 was identified. The strengths ($P_{FE\text{-}0.03}$) of the T-joints corresponding to chord face indentation of 3%d_0 were obtained. It should be noted that four specimens did not reach the chord face indentation value of 3%d_0 due to the brace failed by local buckling. These specimens were marked by $^{\#}$, as shown in Tables 6-8, and they were not used in the further analysis. It should be noted that some specimens experienced chord face indentation of 0.03d_0 but still not reached the peak strength although they were axially loaded with total end shortening of over 50 mm, particularly for those of Series C (see Figures 18-20). Hence, the strengths (P_{FE}) of the T-joints in parametric studies were determined by $P_{FE}=P_{FE\text{-}u}$ if $\mu_u \leq 3\%d_0$; otherwise, $P_{FE}=P_{EF\text{-}0.03}$ if $\mu_u > 3\%d_0$. $P_{EF\text{-}u}$ and μ_u are the ultimate (peak) strengths and the corresponding chord face indentation of an T-joint specimen. Same strength definitions with respect to 3%d_0 have been widely adopted for CHS welded joints in the literature [36-38]. The strengths (P_{FE}) of the T-joints in parametric studies are tabulated in Tables 6-8.

4. Structural performance

4.1 *Deformation capacity and ductility*

The current design guidelines are generally strength-based, but without specifying any requirements for the deformation capacity and ductility of steel tubular joints [59], including those in this study. The chord face indentation limit of 3%d_0 for steel tubular joints was firstly suggested by Lu *et al.* [65], as they found that for the steel tubular joints exhibiting peak loads generally had the chord face indentations within 2.5%d_0 ~ 4%d_0 in the load-deformation curves. Hence, the chord face indentation limit of 3%d_0 was proposed for the steel tubular joints without exhibiting peak loads because of material strain

hardening and membrane action. It should be noted that such limit was based on steel tubular joints made up of normal strength steel, but not for high strength steel. The recent experimental investigation on seven CFHSS CHS T-joints showed that the deformation capacity of the joints could be considered as reasonably sufficient, as evidenced by the indentations at peak loads that were generally at least three times of the respective values of 3%d_0 [59]. In the T-joint specimens [59], the steel tubes used for the chord and brace were press-braked and cold-rolled, respectively, from steel plate with nominal yield stress of 960 MPa.

The ductility of CFHSS members in the T-joint specimens is relatively low with the yield ratio ($f_{0.2}/f_u$) ranging from 0.71 to 0.92 and the fracture strain (ε_f) around 11.0% (see Table 3). However, as also found by Lan *et al*. [59], it is shown that the testing curves all exhibited similar slow-descending without sudden drop of loads after reaching the peak loads (see the test curves of the present study in Figures 5-8). Similar findings were shown in the curves (see Figures 12-20) that were obtained from the parametric studies of this paper, except for those failed by brace local buckling. For the T-joints with chords members of small, medium and large sizes (d_0 = 88.9, 273.0 and 508.0 mm), almost all the curves had not reached the peak loads after experiencing the chord face indentation of 0.03d_0. Larger deformation capacity of these specimens could be anticipated from the figures. Hence, this is favourable for the application of the CFHSS CHS T-joints when the issue of joint deformation and ductility was a concern. Note that this study mainly focusses on the T-joint specimens that failed by chord plastification without preloading in the chords.

4.2 *The effects of geometric parameters*

The effects of geometric parameters on the strengths of CFHSS CHS T-joints failed by chord plastification were analysed. In the investigation of the effects due to the variations of β in each sub-series, the strengths (P_{FE}) were normalized by the strength corresponding to β = 1.00. By following this,

the strengths (P_{FE}) in the sub-series were normalized by 626.7 kN in Table 6 for τ = 1.00 and 2γ = 14.11, and by 3899.2 kN in Table 7 for τ = 0.60 and 2γ = 21.84 and by 4575.0 kN in Table 8 for τ = 0.40 and 2γ = 40.64. Similarly, in the investigation of the effects due to the variations of τ in each sub-series, the values of P_{FE} were normalized by the strength corresponding to τ = 1.00. For those due to the variations of 2γ in each sub-series, the values of P_{FE} were normalized by the strength corresponding to around 2γ = 20. The normalized values for each sub-series are shown in the last columns of Tables 6-8.

The effects of β, τ and 2γ on the joint strengths are plotted in Figures 21-23, respectively. In each figure, the results of the three sub-series from Series A, B and C were used. As shown Figure 21, the T-joint strengths increase as the value of β increase, and the increments are generally larger as the β becomes larger regardless of different sets of τ and 2γ. Furthermore, for each set of τ and 2γ, the trend of strength increments with increasing of β is similar with each other, except that for Series A with τ = 1.00 and 2γ = 14.11, the increments for specimens with β = 0.9 and 1.0 are relatively small as their ultimate strengths occurred near the chord face indentation of $0.03d_0$, which are not the case for the same series with other values of β, and for other series with the same β = 0.9 and 1.0. The joint strengths were not further developed after exceeding the chord face indentation of $0.03d_0$. Hence, the increment of strengths for these two specimens is relatively small.

The variation of τ also has limited effects on the strength of the T-joints for different sets of β and 2γ (see Figure 22). On the contrary to those findings in the effects due to β, the T-joint strengths decrease as the value of 2γ increase, and the decrements are smaller as the 2γ becomes larger regardless of different sets of β and τ. For each set of β and τ, the trend of strength decrements with increasing of 2γ is similar with each other.

5. Strength prediction of existing design rules

371 5.1 *Design guidelines*

372 As discussed in Section 1 of this paper, the strength (*P*) for steel CHS welded joints that failed by
373 chord plastification is function of the 0.2% proof stress (yield strength) together with the square of chord
374 wall thickness ($f_{0.2}t_0^2$) based on the analytical model proposed by Togo in 1967 [58]. The design formulas
375 were developed based on this principle by considering the effects due to the geometrical parameters as
376 represented by Q_u and the preloading condition of the chord by Q_f, which is shown in Equation (3). The
377 angle (θ) between the brace and chord is considered by $sin\theta$, which is equal to 1.0 for all the T-joints in
378 this study. The Q_u and Q_f are determined using multi-regression analyses of the experimental and
379 numerical results. The development of the design equations in the CIDECT and IIW are discussed in
380 detail by Zhao *et al*. [45] and Zhao and Tong [46].

381 $$P = Q_f Q_u \frac{f_{0.2} t_0^2}{\sin\theta} \quad (3)$$

382 The CFHSS CHS T-joints in this study were designed without any preloading in the chords. Hence,
383 the Q_f is equal to 1.0. The determination of Q_u is related to the geometric parameters such as β, τ and 2γ,
384 and generally represented by Equation (4), where *A*, *B*, *and C* are regression coefficients. The parameter
385 of τ is not considered in Equation (4) as it has limited effect on the joint strengths that failed by chord
386 plastification, which is also illustrated in Figure 22 of this paper.

387 $$Q_u = \left(\frac{A}{1-B\beta}\right)(\gamma)^C \quad (4)$$

388 The design guide in CIDECT [52] is generally based on the 3rd edition of the IIW recommendations
389 [49]. It updates the strength equations by considering the chord indentation limit of 3%d_0. Background
390 of the 3rd edition of IIW recommendations [49] is explained by van der Vegte *et al.* [66]. The
391 determination of Q_u in CIDECT [52] is shown in Equation (5), as represented by $Q_{CDT,f}$.

392 $$Q_{CDT,f} = 2.6(1 + 6.8\beta^2)\gamma^{0.2} \quad (5)$$

393 The Equations (3) and (5) provided factored strength of steel CHS T-joints. This is because a safety

394 factor equal to 1.19 has been included [59]. Hence, the nominal strength (unfactored) of T-joints should
395 be determined by Equations (3) and (6).

396 $$Q_{CDT,n} = 3.1(1 + 6.8\beta^2)\gamma^{0.2} \quad (6)$$

397 The validity ranges of the Equation (6) for the steel CHS T-joints are $0.2 \leq \beta \leq 1.0$, $2\gamma \leq 50$ and $\theta \geq$
398 30°. All the CFHSS CHS T-joints in this study had the same $\theta = 90°$, with $0.2 \leq \beta \leq 1.0$ and $10.0 \leq 2\gamma \leq$
399 50.0. The nominal strength calculations in this study, the reduction factor of 0.9 together with the
400 material strength in the minimum of $f_{0.2}$ and $0.8f_u$ were used, as previous numerical studies showed that
401 the predictions overestimated the test strengths for high strength steel circular tubular joints, e.g., X-
402 joints [37,57].

403 The Q_u for steel CHS T-joints in EN 1993-1-8 [55] is, however, mainly based on the 2nd edition of
404 the IIW recommendations [48], which takes the peak loads as the joint strengths. The determination of
405 $Q_{EC,f}$ as specified in Table 7.2 of EN 1993-1-8 [55] is re-written in Equation (7) as shown below:

406 $$Q_{EC,f} = (2.8 + 14.2\beta^2)\gamma^{0.2} \quad (7)$$

407 A partial safety factor (γ_{M5}) equal to 1.0 is suggested for the resistance design in EN 1993-1-8 [55].
408 This is because Equation (7) has implicitly adopted a safety factor of 1.25 [58]. In this sense, the nominal
409 strength of steel CHS T-joints predicted by EN 1993-1-8 [55] should be calculated by Equation (3)
410 together with the nominal $Q_{EC,n}$ as determined by Equation (8).

411 $$Q_{EC,n} = (3.5 + 17.75\beta^2)\gamma^{0.2} \quad (8)$$

412 The Equation (8) is applicable for steel CHS T-joints in the ranges of $0.2 \leq \beta \leq 1.0$, $10.0 \leq 2\gamma \leq 50.0$
413 and $\theta \geq 30°$, as specified in EN 1993-1-8 [55]. The reduction factor of 0.9 is specified [55] for steel with
414 nominal yield strength exceeding 355 MPa and a further reduction factor of 0.8 is specified [2] for steel
415 with nominal yield strength greater than 460 MPa up to 700 MPa. Hence, these two factors were used in
416 the nominal strength calculations in this study.

It should be noted that the Equations (7) and (8) for the Eurocode [55] are developed based on the original Equation (9) proposed by Wardenier [67].

$$Q_W = 4.83(1 + 4.94\beta^2)(2\gamma)^{0.233}(l_0/d_0)^{-0.45} \quad (9)$$

In Equation (9), the effect of bending stresses in the chord is considered by the function of ratio of chord length (l_0) to chord diameter (d_0) for $3 \leq l_0/d_0 \leq 5$. To make a direct comparison, the predictions by using Equation (9) were also assessed in this study, however, the reduction factors were not used for Equation (9).

It should be noted that for the above equations, the brace cross sections of the T-joints are required to be Class 1 or 2 to avoid premature of brace buckling. In this study, the T-joints that failed by brace local buckling before reaching the chord face indentation of 3%d_0 or ultimate load were excluded from the analysis regardless of the brace cross section classifications. The T-joints that failed by chord plastification having chord face indentation of not less than 3%d_0 or reaching clear peak load before such indentation were used to assess the design equations regardless of cross section classifications of the braces. Those 4 specimens (see Tables 6-8) that failed by local buckling of the braces in the T-joints were not included in the analysis in this paper.

5.2 *Comparison of test and numerical strengths with predicted strengths*

The test strengths (P_t) and numerical strengths (P_{FE}) obtained in this study were compared with the nominal strengths predicted by CIDECT [52], EN 1993-1-8 [55] and Wardenier [67], as represented by $P_{CDT,n}$, $P_{EC,n}$ and P_W, respectively. It should be noted that the test strengths (P_t) were taken as $P_{3\%}$ for all the T-joint specimens as the peak loads occurred before the 3%d_0 chord face indentation. The detail comparisons of P_t/P_{CDT}, P_t/P_{EC} and P_t/P_W are shown in Table 9; and those of $P_{FE}/P_{CDT,n}$, $P_{FE}/P_{EC,n}$, and P_{FE}/P_W are shown in Tables 10(a)-(c) for specimen Series A, B and C, respectively.

For the comparisons with the test results, it was found that the current predictions are overall

unconservative. The mean values of $P_t/P_{CDT,n}$, $P_t/P_{EC,n}$ and P_t/P_W are 0.70, 0.93 and 0.68, with the corresponding COVs of 0.095, 0.138 and 0.155 (see Table 9). The reduction factors suggested in CIDECT [52] and EN 1993-1-8 [55] improved the predictions in a less unconservative manner when compared with those predicted by Wardenier [67]. Similarly, the predictions by the design rules are also unconservative when compared with the results obtained from the parametric studies. Generally, the predictions tended to be more unconservative for the joints with larger chord outer diameter (d_0). For example, the mean values of $P_{FE}/P_{CDT,n}$ are 0.78 and 0.66 for specimens Series A and C, respectively, as shown in Tables 10(a) and (c). All these comparisons by using the three design rules are further illustrated in Figures 24-26, respectively. The vertical axis of the figures plots the strength predictions while the horizontal axis plots the test and numerical results. Overall, it was found that the predictions by the current design rules are unconservative. The two specimens with β = 0.9 and 1.0 in Series A (d_0 = 88.9) showed a slight deviation from the trends in predictions (more unconservative), see the triangular legend in Figures 24(b), 25(b) and 26(b), due to their ultimate strengths occurred near the chord face indentation of $0.03d_0$, as discussed earlier. However, it may be concluded that for the small and medium sections (series A and B), the predictions become more unconservative as the values of β increased, as shown in the first sub-series Tables 10(a)-(b).

6. Proposed design rules and predictions

Efforts were made in this session to improve the predictions of the CFHSS CHS T-joints. As discussed earlier, the strength (P) of the T-joints that failed by chord plastification is a function of the $f_{0.2}t_0^2$ (see Equation (3)), and the Q_u (see Equation (4)) that is related to the geometric ratios of β and 2γ, as also illustrated in Figures 21 and 23. Hence, by referring to Equation (6) and Equation (9), both the P_t and P_{FE} in this study were divided by $f_{0.2}t_0^2(2\gamma)^{0.2}$ and $f_{0.2}t_0^2(2\gamma)^{0.233}(L/d)^{-0.45}$. All the results divided by $f_{0.2}t_0^2(2\gamma)^{0.2}$ and $f_{0.2}t_0^2(2\gamma)^{0.233}(L/d)^{-0.45}$ are plotted against the corresponding values of β, as shown in

Figures 27-28, respectively.

It is shown that the values of $P/(f_{0.2}t_0^2(2\gamma)^{0.2})$ and $P/(f_{0.2}t_0^2(2\gamma)^{0.233}(L/d)^{-0.45})$ increased regularly as the values of β increased. However, the values of $P/(f_{0.2}t_0^2(2\gamma)^{0.233}(L/d)^{-0.45})$ were relatively more scattered than those of $P/(f_{0.2}t_0^2(2\gamma)^{0.2})$. Hence, the relationship between $P/(f_{0.2}t_0^2(2\gamma)^{0.2})$ and β were derived and plotted as shown in Figure 27. The relationship of Q_u (represented by Q_P) with β and 2γ was proposed as shown in the following Equation (10).

$$Q_P = (13.3\beta^2 - 4.5\beta + 3.3)(2\gamma)^{0.2} \quad (10)$$

The proposed Equation (10) was used together with Equation (3) to predict the nominal strength (P_P) of the T-joint specimens in this study, as shown in Tables 9-10. The predictions were generally improved when compared with the other three predictions, as the unconservative predictions became conservative or less unconservative. Table 11 further summarized all the comparisons between test and numerical strengths with predictions. Totally, 12 test results and 71 numerical results (the 4 specimens failed by local buckling of the braces but not by chord plastification were not included) were used in the comparisons. Overall, it is shown that all the existing design rules provided unconservative predictions. The EN-1993-1-8 [55] provided the least unconservative predictions with the mean value of 0.91, and least scattered predictions due to the smallest value of COV equal to 0.107. The predictions by using Equation (3) together with the proposed Equation (10) provided improved predictions as reflected in the mean value of 1.01, and comparable COV of 0.107. The comparisons P_P against P_t and P_{FE} are shown in Figure 29. However, the proposed equation provided unconservative strength predictions for the T-joint specimens with small chord diameter of 88.9 mm when β greater than 0.80, as shown in Tables 9-10, and evidenced in Figure 27. Further research works are needed for the strength estimation of T-joint specimens with relatively small chord diameters when β greater than 0.80.

7. Conclusions

Experimental and numerical investigations on cold-formed high strength steel (CFHSS) CHS T-joints have been presented. The CFHSS circular members had nominal 0.2% proof stress ($f_{0.2,n}$) of 1100 MPa. A Total of 12 T-joints were tested by applying axial compression through the brace without preloading in the chord. The T-joints were failed by chord plastification. Non-linear finite element (FE) model was developed for the CFHSS CHS T-joints. Parametric studies were performed by using the verified FE model. The key parameters of β, 2γ and τ were designed in the range of 0.2 to 1.0, 10 to 50 and 0.2 to 1.0, respectively. The T-joints had the outer diameter of the chord (d_0) up to 508 mm. The chord plastification failure of the T-joints was mainly found in the numerical study, which was used in the analysis.

The relationship between the joint strengths and the variation of geometric ratios were investigated. It was found that as the β increased, the joint strengths increased in a similar manner regardless of different sets of τ and 2γ. On the contrary, as the 2γ increased, the joint strengths decreased but still in a similar manner for different sets of β and τ. The variation of τ had limited effects on the joint strengths. The CHFSS CHS T-joins showed good deformation capacity and ductility, particularly for those with d_0 of 273 and 508 mm, as these specimens generally reached the chord face indentation of $0.03d_0$ even they did not reach the peak loads.

The experimental and numerical strengths of the T-joints obtained in this study were used to compare with the predictions by using the existing design rules, including those specified in CIDECT [52] and EN-1993-1-8 [55] as well as those proposed by Wardenier [67]. It was found that the current predictions generally provided unconservative predictions, namely overestimated the CFHSS CHS T-joint strengths. The predictions by EN-1993-1-8 [55] provided the least unconservative predictions. A new equation for Q_P that considering the effects of geometric ratios on the strengths was derived based on both the test

and numerical results. By adopting the newly proposed equation, the predictions were improved (at the conservative side), and provided the least scattered results when compared with the other predictions. However, further research works are needed for the strength estimation of T-joint specimens with relatively small chord diameters when β greater than 0.80, as unconservative strength predictions from the proposed equation are observed. The newly proposed Q_P is generally applicable to the nominal strength predictions of CFHSS CHS T-joints subjected to axial loading in brace without pre-loading in chord. The T-joints are made up of CFHSS CHS tubes with $f_{0.2,n}$ = 1100 MPa, $\theta = 90^o$, β, τ and 2γ ranging from 0.2 to 1.0, 0.2 to 1.0 and 10.0 to 50.0.

Acknowledgements

The authors are grateful to Rautaruukki for supplying the cold-formed high strength steel test specimens. Thanks are due to Wo Lee Steel Co. Ltd. (Hong Kong) for using their welding facilities. The research work described in this paper was supported by a grant from the Research Grants Council of the Hong Kong Special Administrative Region, China (Project No. 17210218).

References

[1] Ma J.L, Chan T.M., Young B. "Tests on high-strength steel hollow sections: a review" Proceedings of the Institution of Civil Engineers-Structures and Buildings 2017; (9)170, 621-630.

[2] EN-1993-1-12. Eurocode 3: design of steel structures - Part 1-12: Additional rules for the extension of EN 1993 up to steel grades S700., EN 1993-1-12 Brussels, Belgium: CEN, 2007.

[3] AISC/AISI. Specification for structural steel buildings., AISC 360–10, Illinois: American Institute of Steel Construction, Chicago, 2010.

[4] AS 4100. Amendment no.1 to AS 4100–1998 steel structures. AS 4100-A1, Australia: Australian Standard; Sydney, Australia, 2012.

[5] Qiang X., Bijlaard F., Kolstein. H. “Post-fire performance of very high strength steel S960”, Journal of Constructional Steel Research 2013; 80, 235-242.

[6] Heidarpour A., Tofts S., Korayem H., Zhao X.L., Hutchinson R. “Mechanical properties of very high strength steel at elevated temperatures”, Fire Safety Journal 2014; 64, 27-35.

[7] Azhari F., Heidarpour A., Zhao X.L. and Hutchinson R. “Mechanical properties of ultra-high strength (Grade 1200) steel tubes under cooling phase of a fire: An experimental investigation”, Construction and Building Materials 2015; 93, 841-850.

[8] Ma J.L., Chan T.M., Young B. “Material properties and residual stresses of cold-formed high strength steel hollow sections”, Journal of Constructional Steel Research 2015; 109, 152-165.

[9] Wang J., Afshan S., Schillo N., Theofanous M., Feldmann M., Gardner L. “Material properties and compressive local buckling response of high strength steel square and rectangular hollow sections”, Engineering Structures 2017; 130, 297-315.

[10] Fang H., Chan, T.M., Young, B. “Material properties and residual stresses of octagonal high strength steel hollow sections”, Journal of Constructional Steel Research 2018; 148, 479-490.

[11] Liu X. Chung K.F. “Experimental and numerical investigation into temperature histories and residual stress distributions of high strength steel S690 welded H-sections”, Engineering Structure 2018; 165, 396-411.

[12] Jiao H., Zhao X.L. “Section slenderness limits of very high strength circular steel tubes in bending”, Thin-Walled Structures 2004; 42(9),1257-71.

552 [13] Wang J., Afshan S., Gkantou M., Theofanous M., Baniotopoulos C., Gardner L. “Flexural
553 behaviour of hot-finished high strength steel square and rectangular hollow sections”, Journal of
554 Constructional Steel Research 2016; 121, 97-109.
555 [14] Ma J.L., Chan T.M., Young B. “Experimental investigation of cold-formed high strength steel
556 tubular beams”, Engineering Structures 2016; 126, 200-209.
557 [15] Ma J.L., Chan T.M., Young B. “Design of cold-formed high strength steel tubular beams”,
558 Engineering Structures 2017; 151, 432-443.
559 [16] Javidan F., Heidarpour A., Zhao X.L., Minkkinen J. “Application of high strength and ultra-high
560 strength steel tubes in long hybrid compressive members: Experimental and numerical investigation”,
561 Thin-Walled Structures 2016; 102, 273-285.
562 [17] Nassirniaa M., Heidarpour A., Zhao X.L., Minkkinen J. “Innovative hollow columns comprising
563 corrugated plates and ultra high-strength steel tubes”, Thin-Walled Structures 2016; 101, 14-25.
564 [18] Wang J., Gardner L. “Flexural buckling of hot-finished high-strength steel SHS and RHS
565 columns”, Journal of Structural Engineering 2017; 143 (6), 04017028.
566 [19] Fang, H., Chan, T.M., Young, B. “Structural performance of cold-formed high strength steel
567 tubular columns”, Engineering Structures 2018; 177, 473-488.
568 [20] Ma J.L., Chan T.M., Young B. “Design of Cold-Formed High-Strength Steel Tubular Stub
569 Columns”, Journal of Structural Engineering 2018; 144(6), 04018063.
570 [21] Fang, H., Chan, T.M., Young, B. “Behavior of Octagonal High-Strength Steel Tubular Stub
571 Columns”, Journal of Structural Engineering 2019; 145(12), 04019150.
572 [22] Fang H., Chan T.M. “Buckling resistance of welded high-strength-steel box-section members
573 under combined compression and bending”, Journal of Constructional Steel
574 Research 2019; 162, 105711.

[23] Su A., Liang Y., Zhao O. “Experimental and numerical studies of S960 ultra-high strength steel welded I-section columns”, Thin-Walled Structures 2020; 107166.

[24] Wang F., Liang Y., Zhao O., Young B. “Pin-ended press-braked S960 ultra-high strength steel angle section columns: Testing, numerical modelling and design”, Engineering Structures 2020; 111418.

[25] Fang H., Chan T.M., Young B. “Experimental and Numerical Investigations of Octagonal High-Strength Steel Tubular Stub Columns under Combined Compression and Bending”, Journal of Structural Engineering 2021; 147(1), 04020282.

[26] Može P., Beg D., Lopatič J. “Net cross-section design resistance and local ductility of elements made of high strength steel”, Journal of Constructional Steel Research 2007; 63 (11), 1431-1441.

[27] Može P., Beg D. “High strength steel tension splices with one or two bolts”, Journal of Constructional Steel Research 2010; 66 (8-9), 1000-1010.

[28] Wang Y.B., Lyu Y.F., Li G.Q., Liew R.J.Y. “Behavior of single bolt bearing on high strength steel plate”, Journal of Constructional Steel Research 2017; 137, 19-30.

[29] Lyu Y.F., Li G.Q., Wang Y.B., Li H., Wang Y.Z. “Bearing behaviour of multi-bolt high strength steel connections”, Engineering Structure 2020; 212, 110510.

[30] Lyu Y.F., Li G.Q., Wang Y.B. “Behavior-Based Resistance Model for Bearing-Type Connection in High-Strength Steels”, Journal of Structure Engineering 2020; 146(7), 04020109.

[31] Jiang K., Zhao O., Tan K.H. “Experimental and numerical study of S700 high strength steel double shear bolted connections in tension”; Engineering Structures 2020; 225, 111175.

[32] Cho Y.H., Teh L.H., Young B., Ahmed A. “Net section tension strength of bolted connections in ultra-high strength sheet steel exposed to fire.” Journal of Constructional Steel Research 2020; 106237.

[33] Cho Y.H., Teh L.H., Ahmed A., Young B. “Material ductility and temperature effects on block shear capacity of bolted connections” Journal of Constructional Steel Research 2020; 106461.

598 [34] Fleischer O., Herion S., Puthli R. “Numerical investigations on the static behaviour of CHS X-
599 joints made of high strength steels”, Tubular Structures XII: Proceedings of Tubular Structures XII,
600 Shanghai, China 2009, pp. 597-605.
601 [35] Puthli R, Bucak O, Herion S, Fleischer O, Fischl A, Josat O. “Adaptation and extension of the
602 valid design formulae for joints made of high-strength steels up to S690 for cold-formed and hot-rolled
603 sections”, CIDECT Report 5BT-7/10 (Draft Final Report) Germany: CIDECT; 2011.
604 [36] Lee C.H., Kim S.H., Chung D.H., Kim D.K., Kim J.W. “Experimental and numerical study of
605 cold-formed high-strength steel CHS X-joints”, Journal of Structure Engineering 2017; 143(8),
606 04017077.
607 [37] Lan X.Y., Chan T.M., Young B. “Static strength of high strength steel CHS X-joints under axial
608 compression”, Journal of Constructional Steel Research 2017; 138, 369-79.
609 [38] Lan X.Y., Chan T.M., Young B. “Structural behaviour and design of chord plastification in high
610 strength steel CHS X-joints”, Construction Building Materials 2018; 191, 1252-67.
611 [39] Lan X.Y., Chan T.M., Young B. “Structural behaviour and design of high strength steel RHS X-
612 joints”, Engineering Structure 2019; 200, 109494.
613 [40] Pandey M., Young B. “Tests of cold-formed high strength steel tubular T-joints”, Thin-Walled
614 Structures 2019; 143, 106200.
615 [41] Pandey M., Young B. “Compression capacities of cold-formed high strength steel tubular T-
616 joints”, Journal of Constructional Steel Research 2019; 162, 105650.
617 [42] Pandey M., Young B. “Structural performance of cold-formed high strength steel tubular X-
618 Joints under brace axial compression”, Engineering Structures 2020; 208, 109768.
619 [43] Su M., Cai Y., Chen X., Young B. “Behaviour of concrete-filled cold-formed high strength steel
620 circular stub columns”, Thin-walled Structures 2020, 157, 107078.

621 [44] Cai Y., Su M., Chen X., Young B. “High strength steel square and rectangular tubular stub
622 columns infilled with concrete”, Journal of Constructional Steel Research 2021, 179, 106536.
623 [45] Zhao X.L., Wardenier J., Packer J.A., van der Vegte G. J. “Current static design guidance for
624 hollow-section joints”, Proceedings of the Institution of Civil Engineers Structures and Buildings 2010;
625 163, 361-373.
626 [46] Zhao X.L., Tong L.W. “New Development in Steel Tubular Joints”, Advances in Structural
627 Engineering 2011; 14(4); 699-715.
628 [47] IIW. Design Recommendations for Hollow Section Joints – Predominantly Statically Loaded,
629 1st Edition, IIW Doc. XV-491- 81, IIW Annual Assembly, Lisbon, Portugal, 1981.
630 [48] IIW. Design Recommendations for Hollow Section Joints – Predominantly Statically Loaded,
631 2nd Edition, IIW Doc. XV- 701-89, IIW Annual Assembly, Helsinki, Finland, 1989.
632 [49] IIW. IIW Static Design Procedure for Welded Hollow Section Joints – Recommendations, IIW
633 Doc. XV-1329–09, IIW Annual Assembly, Singapore, 2009.
634 [50] Wardenier J., Kurobane Y., Packer J.A., Dutta D., Yeomans, N. “Design Guide for Circular
635 Hollow Section (CHS) Joints under Predominantly Static Loading”, TÜV-Verlag, Köln, Germany, 1991.
636 [51] Packer J.A., Wardenier J., Kurobane Y., Dutta D., Yeomans, N. “Design Guide for Rectangular
637 Hollow Section (RHS) Joints under Predominantly Static Loading”, TÜV-Verlag, Köln, Germany, 1992.
638 [52] Wardenier J., Kurobane Y., Packer J.A., van der Vegte G.J., Zhao X.L. “Design Guide for
639 Circular Hollow Section (CHS) Joints under Predominantly Static Loading”, CIDECT Design Guide No.
640 1, 2nd Edition, CIDECT, Geneva, Switzerland, 2008.
641 [53] Packer J.A., Wardenier J., Zhao X.L., van der Vegte G.J., Kurobane, Y. “Design Guide for
642 Rectangular Hollow Section (RHS) Joints under Predominantly Static Loading”, CIDECT Design Guide
643 No. 3, 2nd Edition, CIDECT, Geneva, Switzerland, 2009.

[54] Packer J.A., Henderson J.E. “Hollow Structural Section Connections and Trusses - A Design Guide”, Canadian Institute of Steel Construction (CISC), Willowdale, Ontario, Canada, 1997.

[55] EN 1993-1-8. Eurocode 3: Design of Steel Structures - Part 1.8: Design of Joints, European Committee for Standardization (CEN), Brussels, Belgium, 2005.

[56] BS ISO 14346, Static design procedure for welded hollow-section joints – Recommendations, British Standard International Standards, Geneva, Switzerland, 2013.

[57] Cai Y., Chan T.M., Young B. “Chord plastification in high strength steel circular hollow section X-joints: testing, modelling and strength predictions”, Engineering Structures 2021; In press.

[58] Togo, T. “Experimental study on mechanical behaviour of tubular joints”, Ph.D. Thesis, Osaka University, Japan, (in Japanese), 1967.

[59] Lan X.Y., Chan T.M., Young B. “Experimental study on the behaviour and strength of high strength steel CHS T- and X-joints”, Engineering Structures 2020; 206, 110182

[60] NAS. “North American Specification for the design of cold-formed steel structural members.” North American Specification (NAS), AISI S100–16, Washington D. C., USA: American Iron and Steel Institute (AISI), 2016.

[61] Cai Y., Chan T.M., Young B. “Experimental investigation on cold-formed high strength steel tubular T-joints”, The 9th International Conference on Advances in Steel Structures (ICASS2018), 2018, Hong Kong, China, Paper No. 009, Full paper in drive.

[62] AWS D1.1M. Structural Welding Code-Steel, American Welding Society, AWS D1.1/1.1M, Miami, FL, USA, 2015.

[63] AWS A5.28M. Specification for Low-Alloy Steel Electrodes and Rods for Gas Shielded Arc Welding, American Welding Society, AWS A5.28/A5.28M: 2005, Miami, FL, USA, 2015.

[64] ABAQUS. (2019). “Analysis User’s Manual”, ABAQUS, Inc., Version 6.20, 2019.

667 [65] Lu L.H., de Winkel G.D., Yu Y., Wardenier J. “Deformation limit for the ultimate strength of
668 hollow section joints”, Tubular structures VI. Melbourne: Balkema; 1994. p. 341-347.
669 [66] van der Vegte G.J., Wardenier J, Zhao X.L., Packer J.A. “Evaluation of new CHS strength
670 formulae to design strengths”, Tubular Structures XII. London: CRC Press; 2009; 313-22.
671 [67] Wardenier J. Hollow section joints. The Netherlands: Delft University Press; 1982.

Table 1: Measured dimensions and geometric ratios of CFHSS circular tubular T-joints

Specimens	Brace (mm)			Chord (mm)			Geometric ratios		
Brace - Chord	d_1	t_1	l_1	d_0	t_0	l_0	β	τ	2γ
89×4 - 139×6	89.1	3.93	180.3	137.8	5.95	684.8	0.65	0.66	23.16
108×4 - 139×6	107.8	3.92	218.8	137.9	5.94	703.5	0.78	0.66	23.22
133×4 - 139×6	132.7	3.95	213.9	137.9	5.99	730.5	0.96	0.66	23.02
139×6 - 139×6	138.2	5.96	216.2	137.7	5.98	735.2	1.00	1.00	23.03
89×4 - 133×4	88.6	3.90	179.3	134.2	3.91	665.8	0.66	1.00	34.32
108×4 - 133×4	107.8	3.93	217.9	133.9	3.94	685.4	0.81	1.00	33.98
133×4 - 133×4	133.9	3.93	224.1	133.1	3.93	711.1	1.01	1.00	33.87
89×4 - 108×4	89.2	3.89	179.5	109.3	3.86	591.2	0.82	1.01	28.32
89×4 - 108×4-r	89.3	3.86	179.3	108.4	3.89	591.5	0.82	0.99	27.87
108×4 - 108×4	108.3	3.95	217.5	106.5	3.93	611.2	1.02	1.01	27.10
89×4 - 89×4	89.0	3.88	178.9	88.8	3.88	534.1	1.00	1.00	22.89
89×4 - 89×4-r	89.0	3.89	179.5	88.4	3.89	533.9	1.01	1.00	22.72

Table 2: Measured welding details of the T-joint specimens

Specimens	Δ_1 (mm)	Δ_2 (mm)	Δ_3 (mm)
89×4 - 139×6	6.55	6.15	5.68
108×4 - 139×6	6.10	5.69	5.01
133×4 - 139×6	5.85	5.95	4.57
139×6 - 139×6	5.70	6.50	5.69
89×4 - 133×4	6.35	6.18	5.01
108×4 - 133×4	6.40	6.12	5.32
133×4 - 133×4	6.20	5.99	5.22
89×4 - 108×4	6.00	6.23	4.82
89×4 - 108×4-r	5.65	6.23	5.33
108×4 - 108×4	6.00	5.81	5.40
89×4 - 89×4	6.05	6.19	4.96
89×4 - 89×4-r	6.10	5.84	5.52

Table 3: Measured material properties of CFHSS circular tubes

Sections ($D\times t$)	E	$f_{0.01}$	$f_{0.2}$	f_u	ε_u	ε_f	n	$f_{0.2}/f_u$	$0.8f_u$
mm	GPa	MPa	MPa	MPa	%	%			MPa
89×4[#]	207	585	1213	1313	2.4	10.6	4.1	0.92	1050.4
108×4[#]	203	553	1155	1344	2.3	10.9	4.1	0.86	1075.2
133×4[#]	207	535	1100	1255	2.7	10.7	4.2	0.88	1004.0
139×6	194	486	960	1343	1.6	10.6	4.4	0.71	1074.4

Note: [#] data from Ref. [57].

Table 4: Test results and FE predictions of the T-joints

Specimens	Chord indentation (mm)		Tests (kN)		FEA (kN)		Comparisons	
	$u_{0.03}$	u_u	$P_{3\%}$	P_u	$P_{FE\text{-}1}$	$P_{FE\text{-}u}$	$P_{3\%}/P_{FE\text{-}1}$	$P_u/P_{FE\text{-}u}$
89×4 - 139×6	4.13	7.57	468.2	534.9	443.6	528.9	1.06	1.01
108×4 - 139×6	4.14	6.62	628.1	678.2	562.6	663.8	1.12	1.02
133×4 - 139×6	4.14	5.11	839.5	861.2	811.3	909.8	1.03	0.95
139×6 - 139×6	4.13	5.97	939.6	954.9	875.7	935.7	1.07	1.02
89×4 - 133×4	4.03	7.39	211.0	254.7	191	256.6	1.10	0.99
108×4 - 133×4	4.02	8.24	276.2	323.5	265.3	341.4	1.04	0.95
133×4 - 133×4	3.99	6.06	450.6	472.8	430.1	524.3	1.05	0.90
89×4 - 108×4	3.28	5.82	293.9	320.2	265.8	330.5	1.11	0.97
89×4 - 108×4-r	3.25	5.75	299.5	324.3	272.9	337.6	1.10	0.96
108×4 - 108×4	3.20	4.86	424.2	441.1	397.2	453.9	1.07	0.97
89×4 - 89×4	2.66	3.01	335.8	336.9	357.5	366.7	0.94	0.92
89×4 - 89×4-r	2.65	2.84	332.5	333.7	356.3	364.7	0.93	0.91
						Mean	1.05	0.96
						COV	0.057	0.043

Table 5: Specimens of CFHSS circular tubular T-joints in parametric studies

Series	Chord (mm)		Brace (mm)		Geometric ratios		
	d_0	t_0	d_1	t_1	B	τ	2γ
Series A	88.90	6.30	[17.78~88.90]	6.30	[0.20~1.00]	1.00	14.11
		6.30	35.56	[1.26~6.30]	0.40	[0.20~1.00]	14.11
		[1.78~8.89]	35.56	[1.78~8.89]	0.40	1.00	[10.00~50.00]
Series B	273.00	12.50	[54.60~273.00]	7.50	[0.20~1.00]	0.60	21.84
		12.50	163.80	[2.50~12.50]	0.60	[0.20~1.00]	21.84
		[5.46~27.30]	163.80	[3.28~16.38]	0.60	0.60	[10.00~50.00]
Series C	508.00	12.50	[101.60~508.00]	5.00	[0.20~1.00]	0.40	40.64
		12.50	406.40	[2.50~12.50]	0.80	[0.20~1.00]	40.64
		[10.16~50.80]	406.40	[4.06~20.32]	0.80	0.40	[10.00~50.00]

Table 6: Parametric study results and strength comparisons for T-joints Series A (d_0 = 88.9 mm)

Specimens	Geometric ratios			P_{FE}	Normalized
Brace-Chord	β	τ	2γ	(kN)	
17.78×6.30 - 88.90×6.30	0.20	1.00	14.11	221.4	0.35
26.67×6.30 - 88.90×6.30	0.30	1.00	14.11	267.8	0.43
35.56×6.30 - 88.90×6.30	0.40	1.00	14.11	320.4	0.51
44.45×6.30 - 88.90×6.30	0.50	1.00	14.11	379.8	0.61
53.34×6.30 - 88.90×6.30	0.60	1.00	14.11	445.5	0.71
62.23×6.30 - 88.90×6.30	0.70	1.00	14.11	514.7	0.82
71.12×6.30 - 88.90×6.30	0.80	1.00	14.11	583.2	0.93
80.01×6.30 - 88.90×6.30	0.90	1.00	14.11	620.4	0.99
88.90×6.30 - 88.90×6.30	1.00	1.00	14.11	626.7	1.00
35.56×1.26 - 88.90×6.30#	0.40	0.20	14.11	-	-
35.56×1.89 - 88.90×6.30#	0.40	0.30	14.11	-	-
35.56×2.52 - 88.90×6.30	0.40	0.40	14.11	309.1	0.96
35.56×3.15 - 88.90×6.30	0.40	0.50	14.11	315.0	0.98
35.56×3.78 - 88.90×6.30	0.40	0.60	14.11	316.9	0.99
35.56×4.41 - 88.90×6.30	0.40	0.70	14.11	318.1	0.99
35.56×5.04 - 88.90×6.30	0.40	0.80	14.11	319.0	1.00
35.56×5.67 - 88.90×6.30	0.40	0.90	14.11	319.8	1.00
35.56×6.30 - 88.90×6.30	0.40	1.00	14.11	320.4	1.00
35.56×1.78 - 88.90×1.78	0.40	1.00	49.94	25.5	0.16
35.56×1.98 - 88.90×1.98	0.40	1.00	44.90	31.5	0.20
35.56×2.22 - 88.90×2.22	0.40	1.00	40.05	39.7	0.25
35.56×2.54 - 88.90×2.54	0.40	1.00	35.00	52.1	0.32
35.56×2.96 - 88.90×2.96	0.40	1.00	30.03	71.1	0.44
35.56×3.56 - 88.90×3.56	0.40	1.00	24.97	103.1	0.64
35.56×4.45 - 88.90×4.45	0.40	1.00	19.98	161.5	1.00
35.56×6.30 - 88.90×6.30	0.40	1.00	14.11	320.4	1.98
35.56×8.89 - 88.90×8.89	0.40	1.00	10.00	608.5	3.77

Note: # means brace failed in local buckling.

Table 7: Parametric study results and strength comparisons for T-joints Series B (d_0 = 273.0 mm)

Specimens	Geometric ratios			P_{FE}	Normalized
Brace-Chord	β	τ	2γ	(kN)	
54.60×7.50 - 273.00×12.50	0.20	0.60	21.84	868.8	0.22
81.90×7.50 - 273.00×12.50	0.30	0.60	21.84	1086.2	0.28
109.20×7.50 - 273.00×12.50	0.40	0.60	21.84	1328.9	0.34
136.50×7.50 - 273.00×12.50	0.50	0.60	21.84	1604.8	0.41
163.80×7.50 - 273.00×12.50	0.60	0.60	21.84	1924.5	0.49
191.10×7.50 - 273.00×12.50	0.70	0.60	21.84	2305.1	0.59
218.40×7.50 - 273.00×12.50	0.80	0.60	21.84	2563.5	0.66
245.70×7.50 - 273.00×12.50	0.90	0.60	21.84	3339.6	0.86
273.00×7.50 - 273.00×12.50	1.00	0.60	21.84	3899.2	1.00
163.80×2.50 - 273.00×12.50#	0.60	0.20	21.84	-	-
163.80×3.75 - 273.00×12.50	0.60	0.30	21.84	1815.3	0.93
163.80×5.00 - 273.00×12.50	0.60	0.40	21.84	1876.3	0.96
163.80×6.25 - 273.00×12.50	0.60	0.50	21.84	1906.2	0.97
163.80×7.50 - 273.00×12.50	0.60	0.60	21.84	1924.5	0.98
163.80×8.75 - 273.00×12.50	0.60	0.70	21.84	1936.8	0.99
163.80×10.00 - 273.00×12.50	0.60	0.80	21.84	1946.0	0.99
163.80×11.25 - 273.00×12.50	0.60	0.90	21.84	1952.2	1.00
163.80×12.50 - 273.00×12.50	0.60	1.00	21.84	1956.8	1.00
163.80×3.28 - 273.00×5.46	0.60	0.60	50.00	483.3	0.25
163.80×3.64 - 273.00×6.07	0.60	0.60	44.98	567.8	0.30
163.80×4.10 - 273.00×6.83	0.60	0.60	39.97	681.6	0.35
163.80×4.68 - 273.00×7.80	0.60	0.60	35.00	842.7	0.44
163.80×5.46 - 273.00×9.10	0.60	0.60	30.00	1090.2	0.57
163.80×6.55 - 273.00×10.92	0.60	0.60	25.00	1502.5	0.78
163.80×7.50 - 273.00×12.50	0.60	0.60	21.84	1924.5	1.00
163.80×10.92 - 273.00×18.20	0.60	0.60	15.00	3880.5	2.02
163.80×16.38 - 273.00×27.30	0.60	0.60	10.00	7799.9	4.05

Note: # means brace failed in local buckling.

Table 8: Parametric study results and strength comparisons for T-joints Series C (d_0 = 508.0 mm)

Specimens	Geometric ratios			P_{FE}	Normalized
Brace - Chord	β	τ	2γ	(kN)	
101.60×5.00 - 508.00×12.50	0.20	0.40	40.64	839.5	0.18
152.40×5.00 - 508.00×12.50	0.30	0.40	40.64	1096.9	0.24
203.20×5.00 - 508.00×12.50	0.40	0.40	40.64	1377.5	0.30
254.00×5.00 - 508.00×12.50	0.50	0.40	40.64	1666.7	0.36
304.80×5.00 - 508.00×12.50	0.60	0.40	40.64	1986.1	0.43
355.60×5.00 - 508.00×12.50	0.70	0.40	40.64	2369.9	0.52
406.40×5.00 - 508.00×12.50	0.80	0.40	40.64	2889.6	0.63
457.20×5.00 - 508.00×12.50	0.90	0.40	40.64	3598.1	0.79
508.00×5.00 - 508.00×12.50	1.00	0.40	40.64	4575.0	1.00
406.40×2.50 - 508.00×12.50#	0.80	0.20	40.64	-	-
406.40×3.75 - 508.00×12.50	0.80	0.30	40.64	2828.6	0.93
406.40×5.00 - 508.00×12.50	0.80	0.40	40.64	2889.6	0.95
406.40×6.25 - 508.00×12.50	0.80	0.50	40.64	2925.7	0.97
406.40×7.50 - 508.00×12.50	0.80	0.60	40.64	2954.7	0.98
406.40×8.75 - 508.00×12.50	0.80	0.70	40.64	2979.0	0.98
406.40×10.00 - 508.00×12.50	0.80	0.80	40.64	3000.1	0.99
406.40×11.25 - 508.00×12.50	0.80	0.90	40.64	3016.5	1.00
406.40×12.50 - 508.00×12.50	0.80	1.00	40.64	3029.8	1.00
406.40×4.06 - 508.00×10.16	0.80	0.40	50.00	2081.4	0.20
406.40×4.52 - 508.00×11.29	0.80	0.40	45.00	2450.3	0.23
406.40×5.00 - 508.00×12.50	0.80	0.40	40.64	2889.6	0.28
406.40×5.81 - 508.00×14.51	0.80	0.40	35.01	3725.9	0.36
406.40×6.77 - 508.00×16.93	0.80	0.40	30.01	4911.7	0.47
406.40×8.13 - 508.00×20.32	0.80	0.40	25.00	6875.0	0.66
406.40×10.16 - 508.00×25.40	0.80	0.40	20.00	10466.5	1.00
406.40×13.55 - 508.00×33.87	0.80	0.40	15.00	17517.7	1.67
406.40×20.32 - 508.00×50.80	0.80	0.40	10.00	32003.6	3.06

Note: # means brace failed in local buckling.

Table 9: Strength comparisons between test results and predictions

Specimens	$P_t/P_{CDT,n}$	$P_t/P_{EC,n}$	P_t/P_W	P_t/P_P
89×4 - 139×6	0.79	1.07	0.86	1.23
108×4 - 139×6	0.79	1.10	0.79	1.25
133×4 - 139×6	0.73	1.04	0.75	1.15
139×6 - 139×6	0.77	1.09	0.79	1.20
89×4 - 133×4	0.70	0.88	0.63	1.01
108×4 - 133×4	0.67	0.85	0.61	0.96
133×4 - 133×4	0.75	0.97	0.70	1.07
89×4 - 108×4	0.70	0.91	0.66	1.03
89×4 - 108×4-r	0.69	0.90	0.65	1.02
108×4 - 108×4	0.68	0.90	0.65	0.99
89×4 - 89×4	0.60	0.74	0.53	0.81
89×4 - 89×4-r	0.58	0.72	0.52	0.79
Mean	0.70	0.93	0.68	1.04
COV	0.095	0.138	0.155	0.143

Table 10: Strength comparisons between parametric study results and predictions

(a) Series A with d_0 = 88.9 mm

Specimens	$P_{FE}/P_{CDT,n}$	$P_{FE}/P_{EC,n}$	P_{FE}/P_W	P_{FE}/P_P
17.78×6.30 - 88.90×6.30	0.99	1.08	0.78	0.97
26.67×6.30 - 88.90×6.30	0.94	1.08	0.78	1.09
35.56×6.30 - 88.90×6.30^	0.87	1.04	0.75	1.13
44.45×6.30 - 88.90×6.30	0.80	0.98	0.71	1.12
53.34×6.30 - 88.90×6.30	0.73	0.92	0.66	1.06
62.23×6.30 - 88.90×6.30	0.68	0.86	0.62	0.99
71.12×6.30 - 88.90×6.30	0.62	0.80	0.58	0.91
80.01×6.30 - 88.90×6.30	0.54	0.71	0.51	0.80
88.90×6.30 - 88.90×6.30	0.46	0.60	0.44	0.67
35.56×1.26 - 88.90×6.30#	-	-	-	-
35.56×1.89 - 88.90×6.30#	-	-	-	-
35.56×2.52 - 88.90×6.30	0.84	1.00	0.72	1.09
35.56×3.15 - 88.90×6.30	0.86	1.02	0.73	1.12
35.56×3.78 - 88.90×6.30	0.86	1.02	0.74	1.12
35.56×4.41 - 88.90×6.30	0.87	1.03	0.74	1.13
35.56×5.04 - 88.90×6.30	0.87	1.03	0.74	1.13
35.56×5.67 - 88.90×6.30	0.87	1.03	0.74	1.13
35.56×6.30 - 88.90×6.30^	0.87	1.04	0.75	1.13
35.56×1.78 - 88.90×1.78	0.68	0.80	0.58	0.88
35.56×1.98 - 88.90×1.98	0.69	0.82	0.59	0.90
35.56×2.22 - 88.90×2.22	0.71	0.84	0.60	0.92
35.56×2.54 - 88.90×2.54	0.73	0.86	0.62	0.95
35.56×2.96 - 88.90×2.96	0.75	0.89	0.64	0.98
35.56×3.56 - 88.90×3.56	0.78	0.93	0.67	1.02
35.56×4.45 - 88.90×4.45	0.82	0.98	0.70	1.07
35.56×6.30 - 88.90×6.30^	0.87	1.04	0.75	1.13
35.56×8.89 - 88.90×8.89	0.89	1.06	0.76	1.16
Mean	0.78	0.93	0.67	1.01
COV	0.165	0.134	0.134	0.125

Note: # means brace failed in local buckling; ^ means identical specimens.

(b) Series B with d_0 = 273.0 mm

Specimens	$P_{FE}/P_{CDT,n}$	$P_{FE}/P_{EC,n}$	P_{FE}/P_W	P_{FE}/P_P
54.60×7.50 - 273.00×12.50	0.90	0.98	0.71	0.89
81.90×7.50 - 273.00×12.50	0.89	1.02	0.73	1.03
109.20×7.50 - 273.00×12.50	0.84	1.00	0.72	1.10
136.50×7.50 - 273.00×12.50	0.79	0.96	0.69	1.10
163.80×7.50 - 273.00×12.50^	0.74	0.93	0.67	1.07
191.10×7.50 - 273.00×12.50	0.70	0.90	0.65	1.03
218.40×7.50 - 273.00×12.50	0.63	0.82	0.59	0.93
245.70×7.50 - 273.00×12.50	0.68	0.89	0.64	1.00
273.00×7.50 - 273.00×12.50	0.66	0.88	0.63	0.96
163.80×2.50 - 273.00×12.50#	-	-	-	-
163.80×3.75 - 273.00×12.50	0.70	0.88	0.63	1.01
163.80×5.00 - 273.00×12.50	0.72	0.91	0.65	1.04
163.80×6.25 - 273.00×12.50	0.73	0.92	0.66	1.06
163.80×7.50 - 273.00×12.50^	0.74	0.93	0.67	1.07
163.80×8.75 - 273.00×12.50	0.74	0.93	0.67	1.08
163.80×10.00 - 273.00×12.50	0.75	0.94	0.68	1.08
163.80×11.25 - 273.00×12.50	0.75	0.94	0.68	1.08
163.80×12.50 - 273.00×12.50	0.75	0.94	0.68	1.09
163.80×3.28 - 273.00×5.46	0.82	1.04	0.75	1.19
163.80×3.64 - 273.00×6.07	0.80	1.01	0.72	1.16
163.80×4.10 - 273.00×6.83	0.78	0.98	0.70	1.12
163.80×4.68 - 273.00×7.80	0.76	0.95	0.68	1.09
163.80×5.46 - 273.00×9.10	0.74	0.93	0.67	1.07
163.80×6.55 - 273.00×10.92	0.74	0.92	0.67	1.06
163.80×7.50 - 273.00×12.50^	0.74	0.93	0.67	1.07
163.80×10.92 - 273.00×18.20	0.76	0.95	0.69	1.10
163.80×16.38 - 273.00×27.30	0.73	0.92	0.66	1.06
Mean	0.75	0.94	0.68	1.06
COV	0.085	0.052	0.052	0.063

Note: # means brace failed in local buckling; ^ means identical specimens.

(c) Series C with d_0 = 508.0 mm

Specimens	$P_{FE}/P_{CDT,n}$	$P_{FE}/P_{EC,n}$	P_{FE}/P_W	P_{FE}/P_P
101.60×5.00 - 508.00×12.50	0.77	0.84	0.60	0.76
152.40×5.00 - 508.00×12.50	0.79	0.91	0.65	0.92
203.20×5.00 - 508.00×12.50	0.77	0.92	0.66	1.00
254.00×5.00 - 508.00×12.50	0.72	0.88	0.64	1.01
304.80×5.00 - 508.00×12.50	0.67	0.85	0.61	0.97
355.60×5.00 - 508.00×12.50	0.64	0.82	0.59	0.94
406.40×5.00 - 508.00×12.50^	0.63	0.82	0.59	0.93
457.20×5.00 - 508.00×12.50	0.65	0.85	0.61	0.95
508.00×5.00 - 508.00×12.50	0.69	0.91	0.65	1.00
406.40×2.50 - 508.00×12.50#	-	-	-	-
406.40×3.75 - 508.00×12.50	0.62	0.80	0.58	0.91
406.40×5.00 - 508.00×12.50^	0.63	0.82	0.59	0.93
406.40×6.25 - 508.00×12.50	0.64	0.83	0.60	0.94
406.40×7.50 - 508.00×12.50	0.64	0.84	0.60	0.95
406.40×8.75 - 508.00×12.50	0.65	0.84	0.61	0.96
406.40×10.00 - 508.00×12.50	0.65	0.85	0.61	0.96
406.40×11.25 - 508.00×12.50	0.66	0.86	0.62	0.97
406.40×12.50 - 508.00×12.50	0.66	0.86	0.62	0.97
406.40×4.06 - 508.00×10.16	0.66	0.86	0.62	0.97
406.40×4.52 - 508.00×11.29	0.64	0.83	0.60	0.95
406.40×5.00 - 508.00×12.50^	0.63	0.82	0.59	0.93
406.40×5.81 - 508.00×14.51	0.62	0.81	0.58	0.92
406.40×6.77 - 508.00×16.93	0.62	0.81	0.58	0.92
406.40×8.13 - 508.00×20.32	0.63	0.81	0.59	0.92
406.40×10.16 - 508.00×25.40	0.64	0.83	0.60	0.94
406.40×13.55 - 508.00×33.87	0.64	0.83	0.59	0.94
406.40×20.32 - 508.00×50.80	0.56	0.73	0.52	0.82
Mean	0.66	0.84	0.61	0.94
COV	0.082	0.047	0.047	0.058

Note: # means brace failed in local buckling; ^ means identical specimens.

Table 11: Overall comparisons of test and numerical results with predictions

Specimens	Test + FEA		$P_t/P_{CDT,n}$ ($P_{FE}/P_{CDT,n}$)	$P_t/P_{EC,n}$ ($P_{FE}/P_{EC,n}$)	P_t/P_W (P_{FE}/P_W)	P_t/P_P (P_{FE}/P_P)
Total	12 + 71	Mean	0.73	0.91	0.65	1.01
		COV	0.132	0.107	0.111	0.107

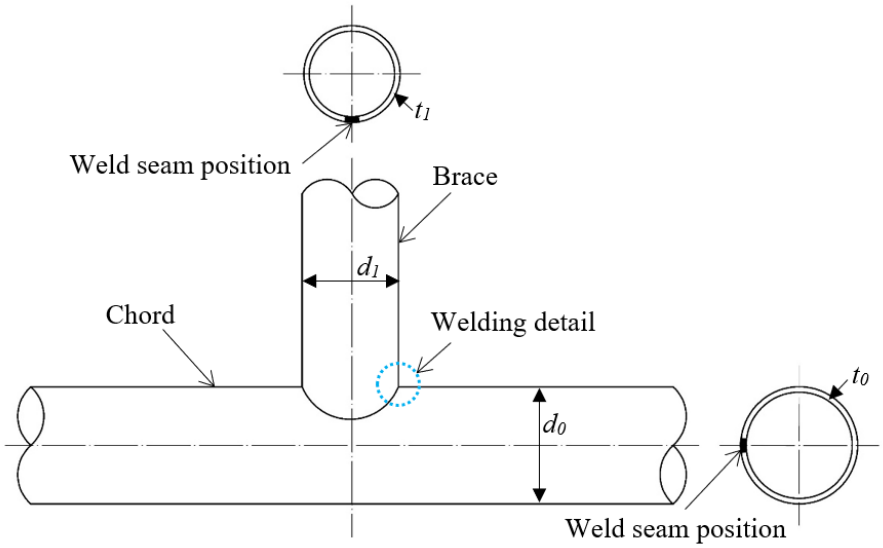

(a) Schematic view

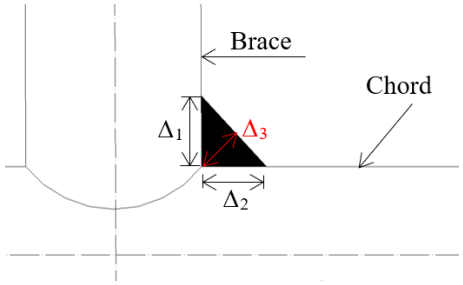

(b) Welding detail

Figure 1: Schematic view and welding detail of CFHSS circular tubular T-joint

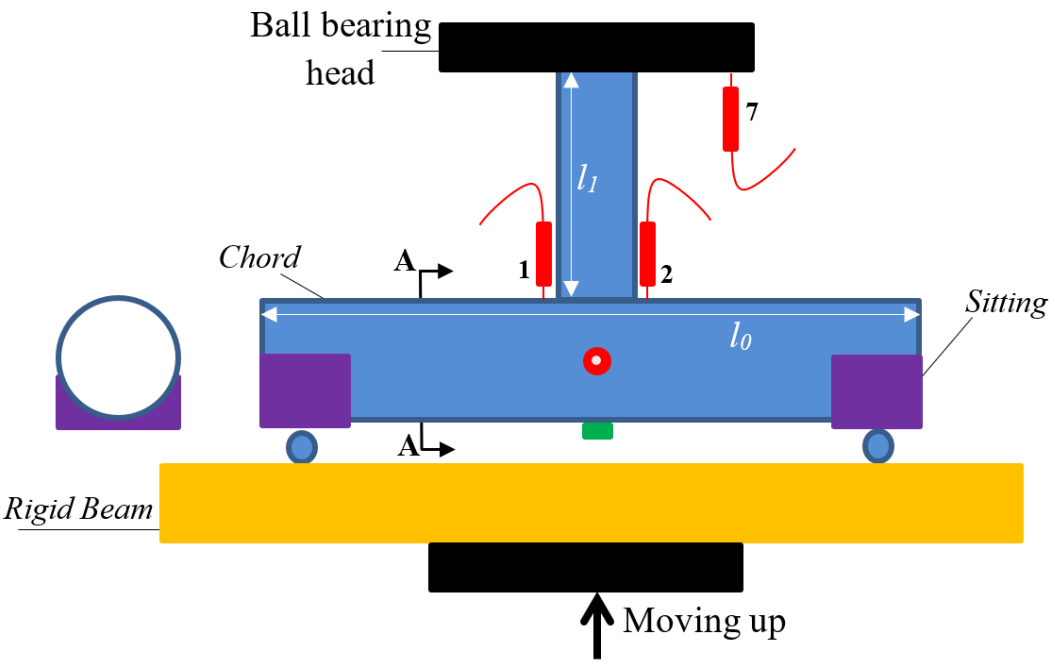

(a) Elevation view of T-joint set up

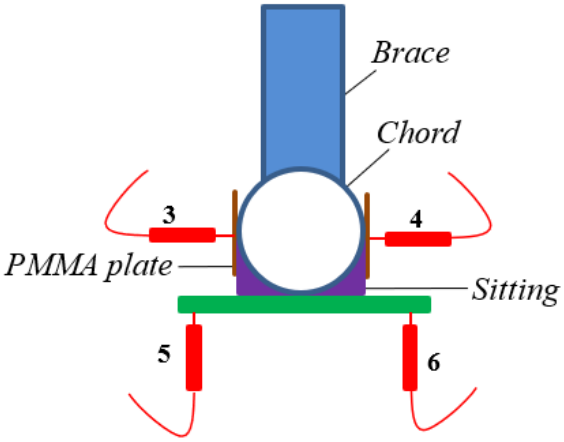

(b) Details of Section A-A

Figure 2: Schematic view of test setup for CFHSS circular tubular T-joint

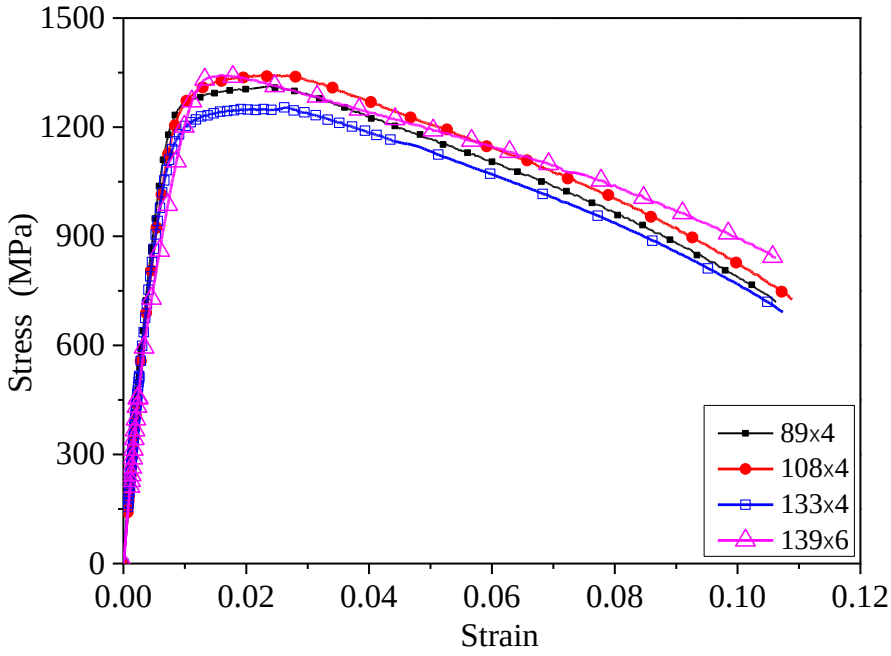

Figure 3: Static stress-strain curves of CFHSS circular tubes

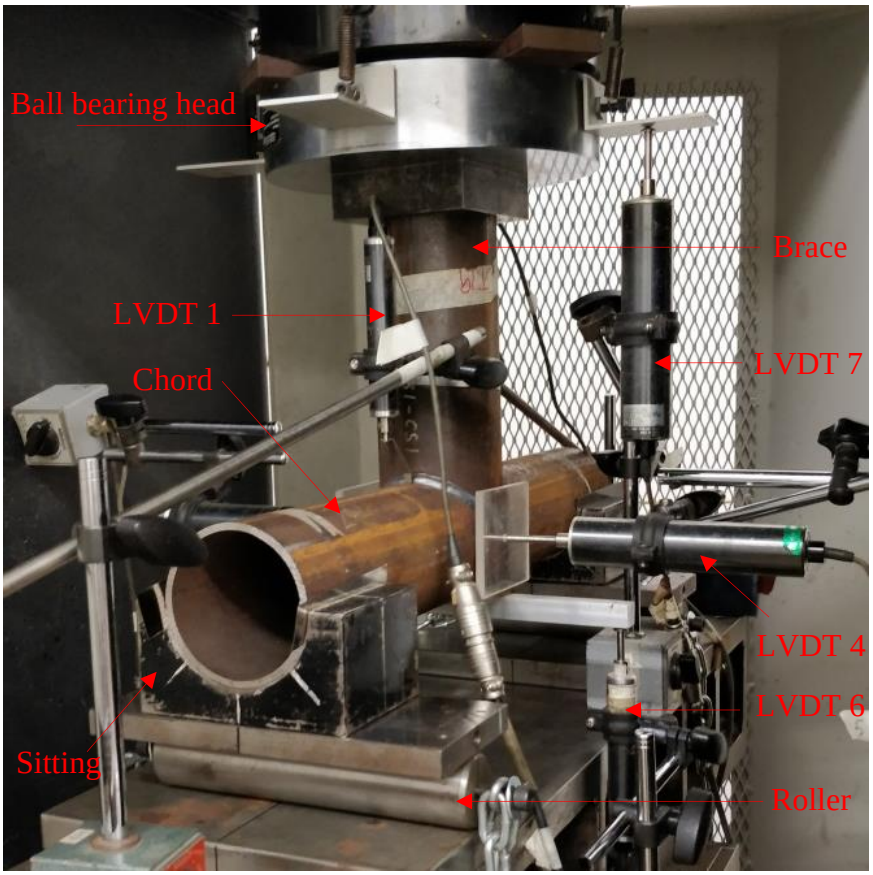

Figure 4: Photo of test setup for the T-joint specimen 89×4 - 89×4

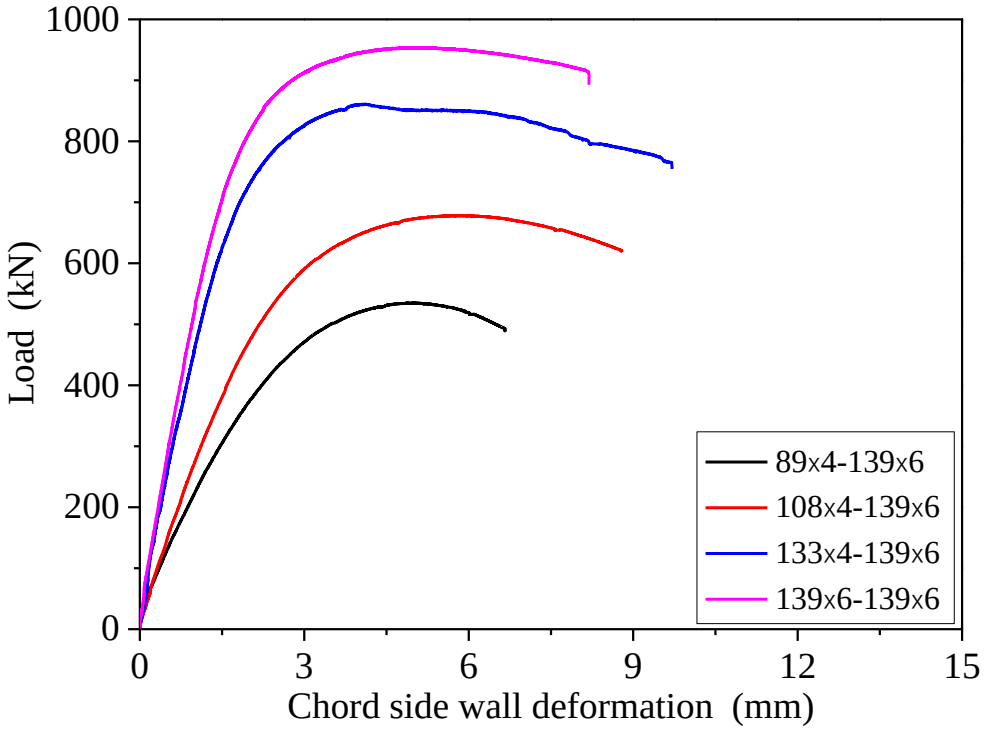

(a) Load-chord side wall deformation curves

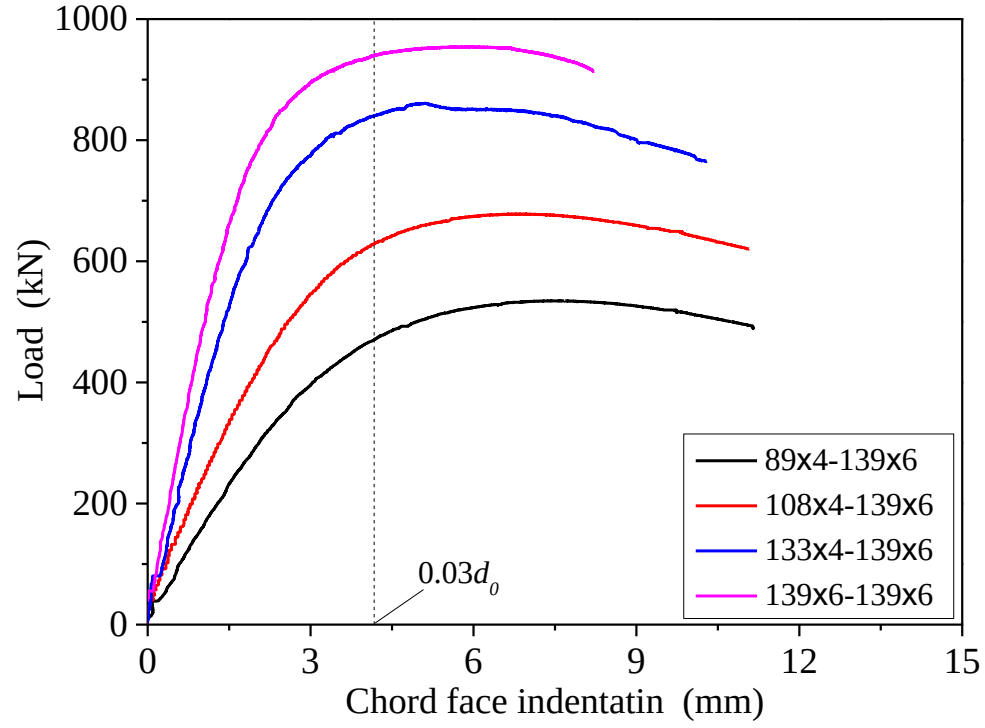

(b) Load-chord face indentation curves

Figure 5: Test curves of T-joints with chord of 139×6 mm

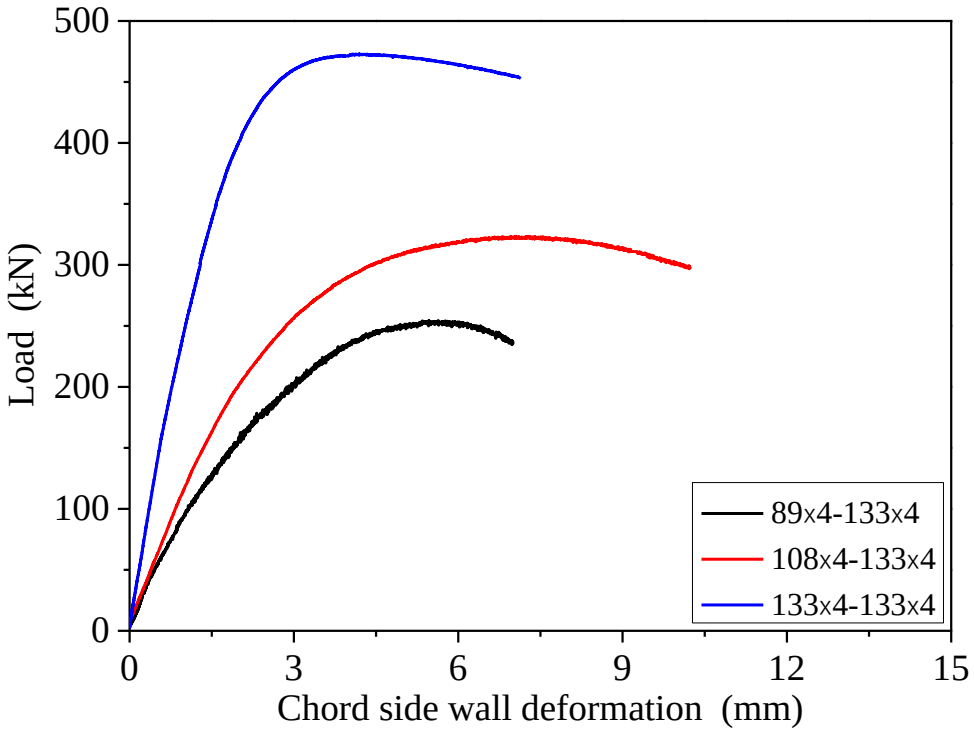

(a) Load-chord side wall deformation curves

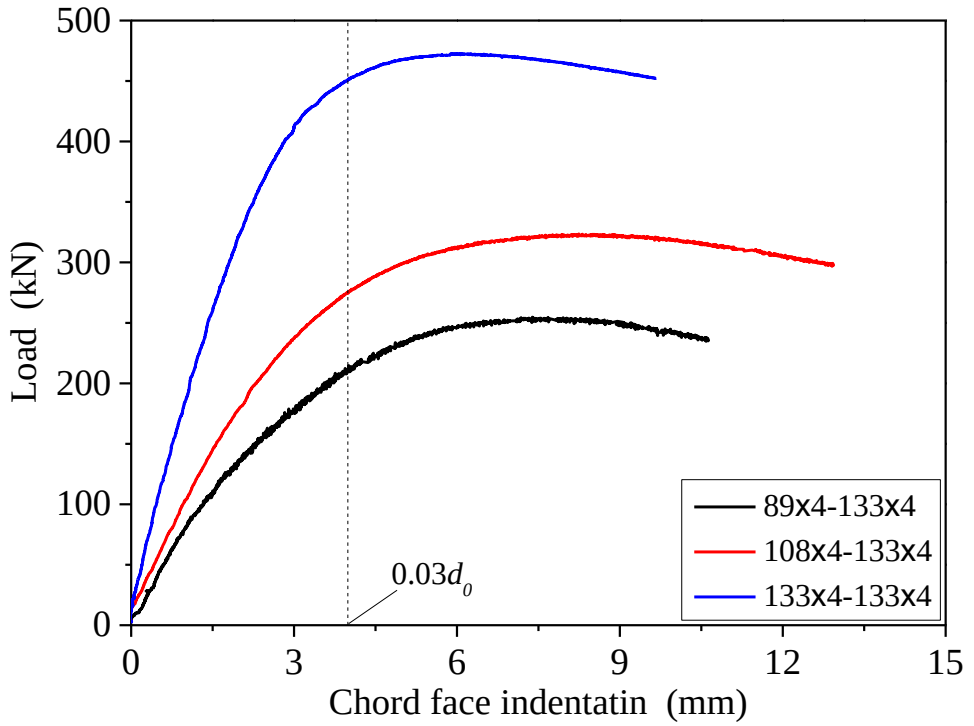

(b) Load-chord face indentation curves

Figure 6: Test curves of T-joints with chord of 133×4 mm

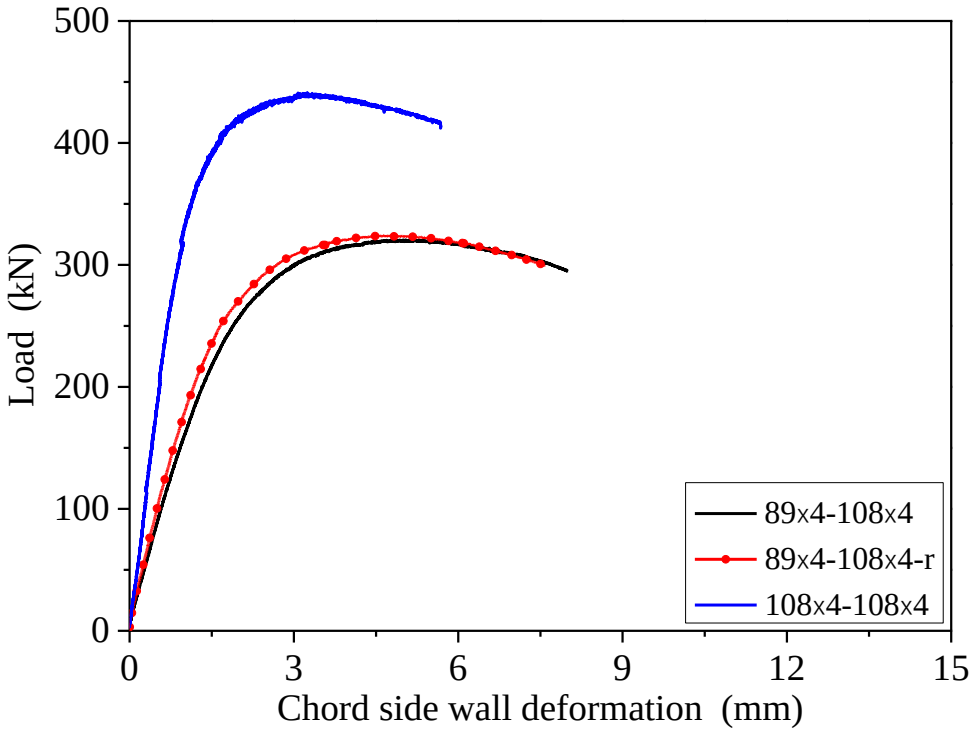

(a) Load-chord side wall deformation curves

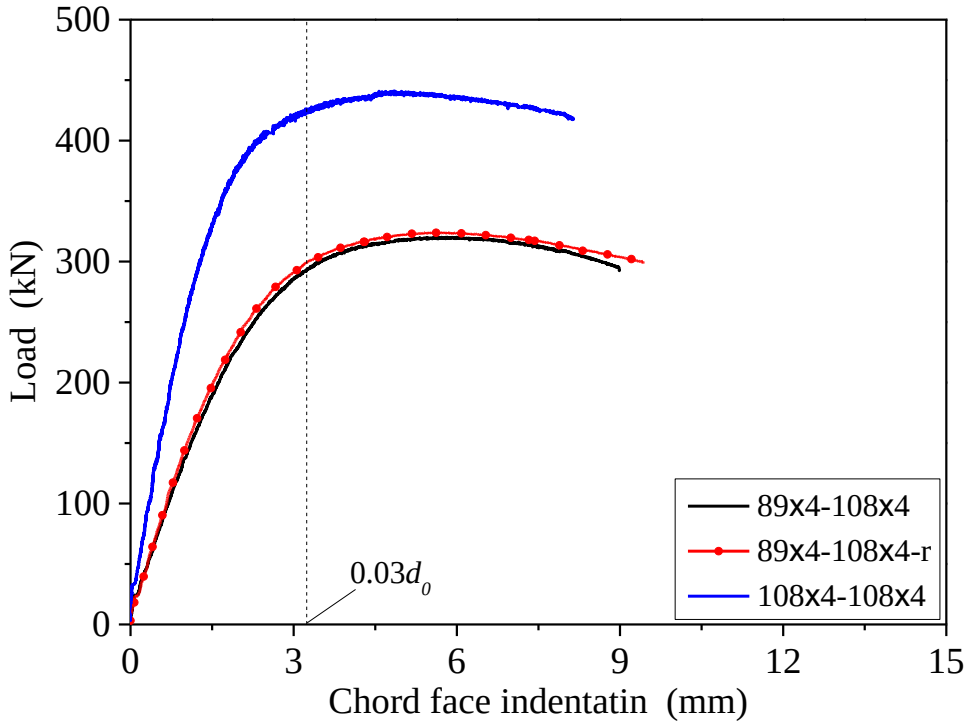

(b) Load-chord face indentation curves

Figure 7: Test curves of T-joints with chord of 108×4 mm

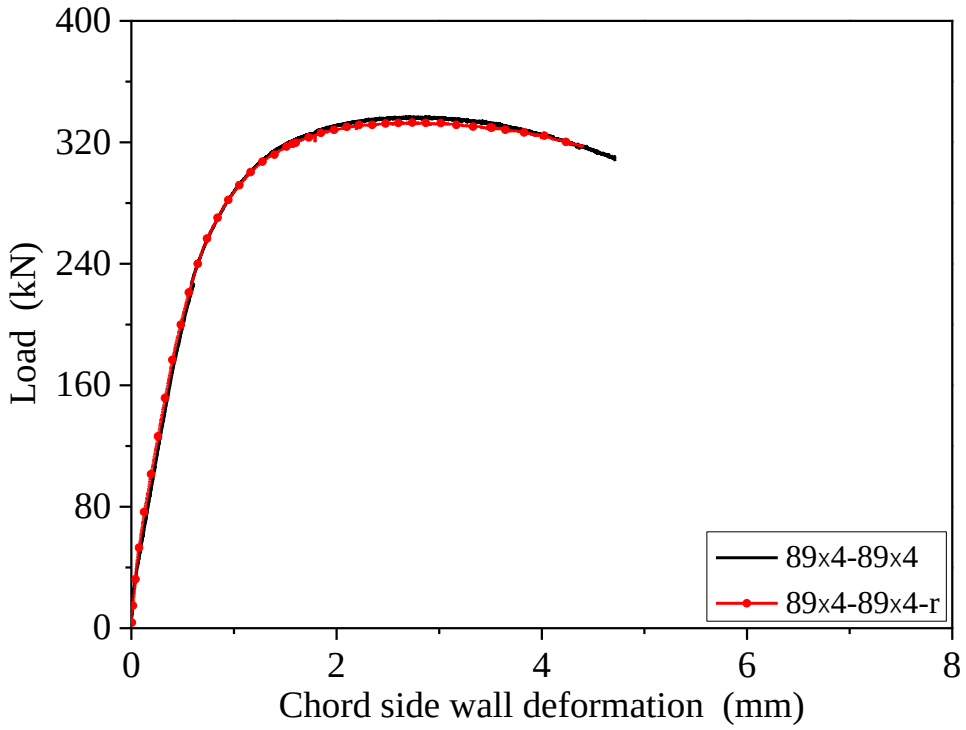

(a) Load-chord side wall deformation curves

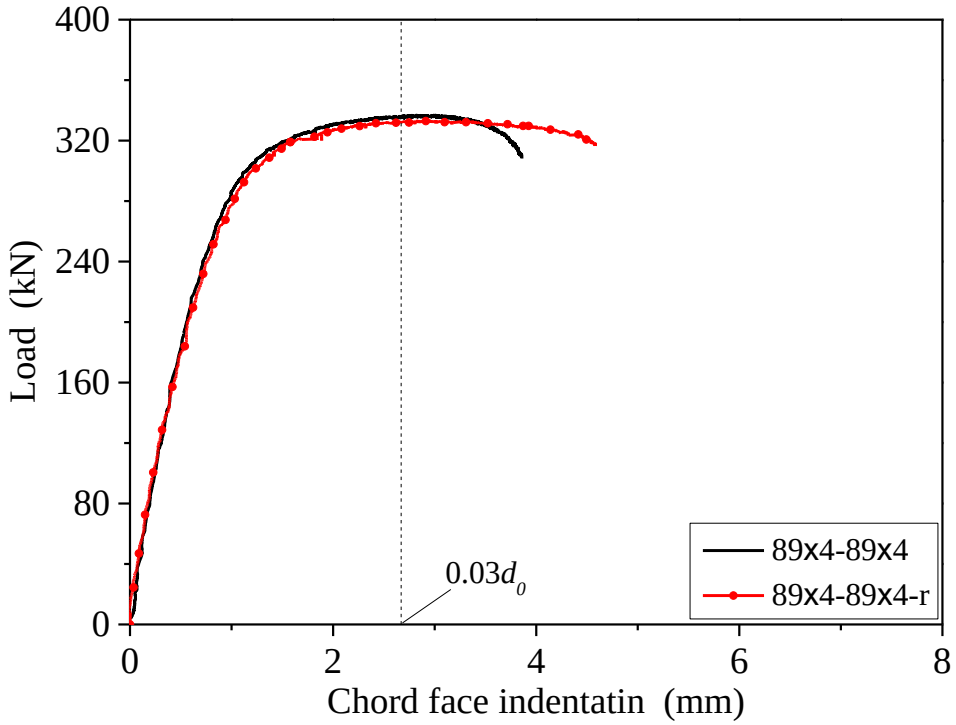

(b) Load-chord face indentation curves

Figure 8: Test curves of T-joints with chord of 89×4 mm

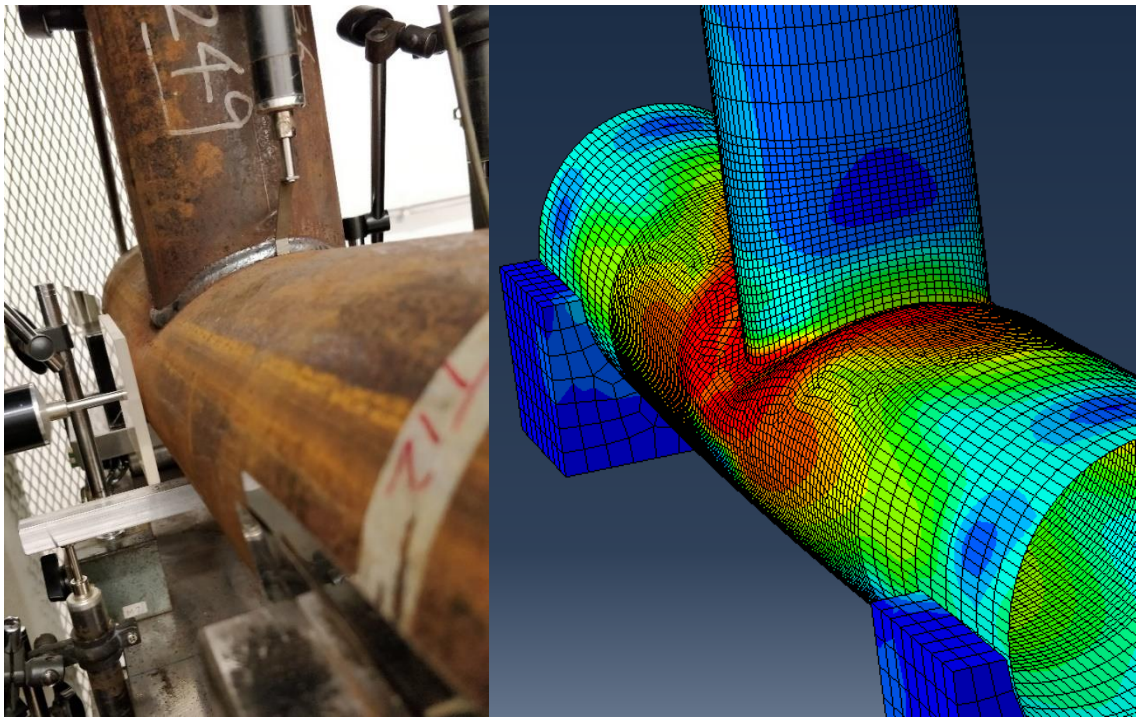

(a) Comparison of failure mode between test and FE results

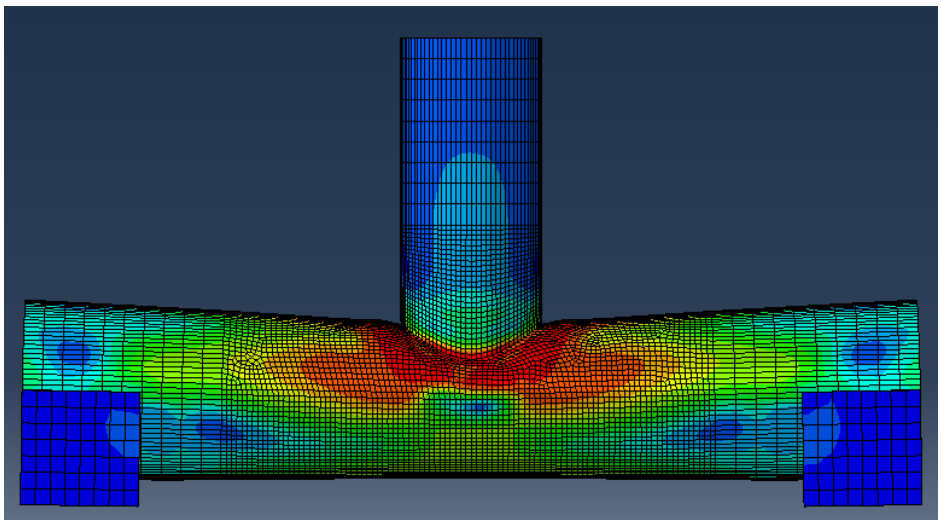

(b) Side elevation view of FE result

Figure 9: Chord plastification failure of T-joint specimen 108×4 - 133×4

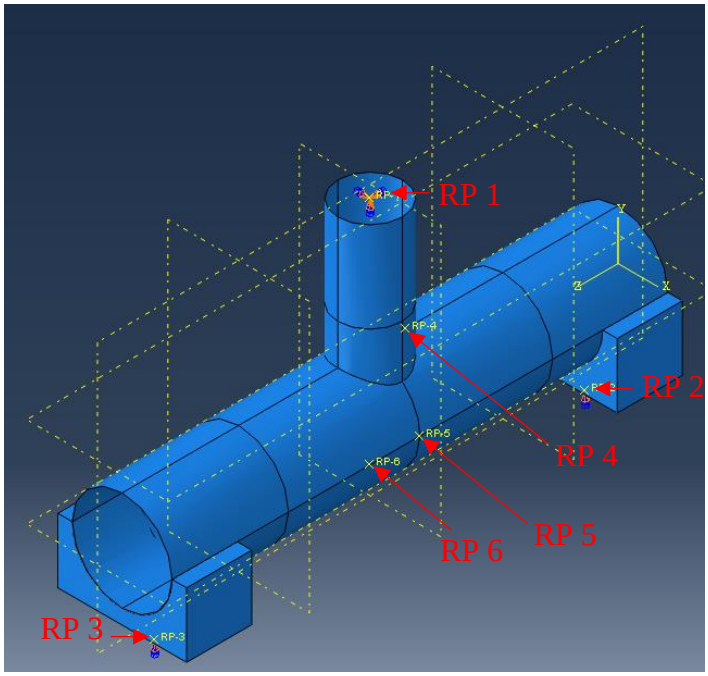

(a) 3-D view of FE model

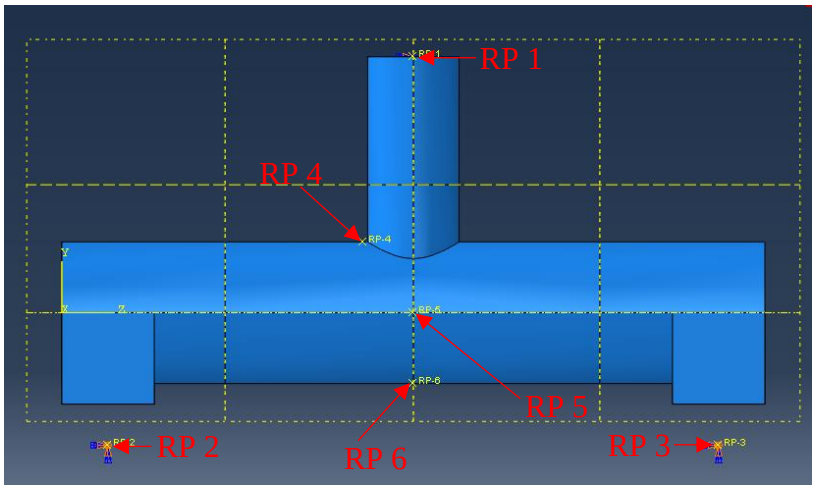

(b) Side view of FE model

Figure 10: FE model of CFHSS T-joint specimen 89×4 - 139×6

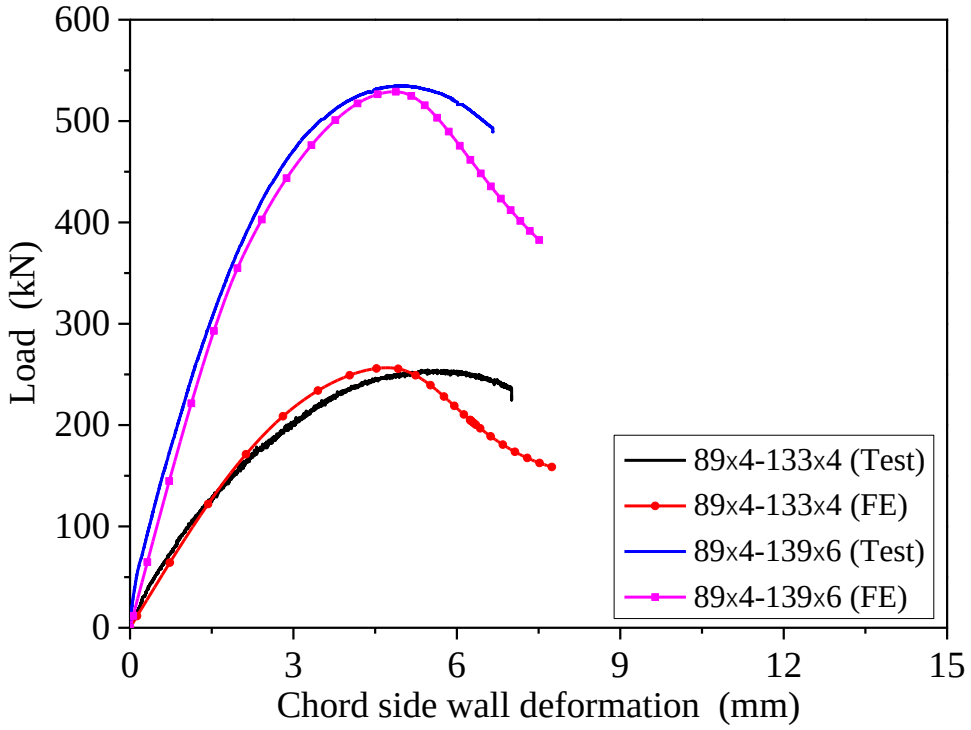

(a) Comparison of load-chord side wall deformation curves

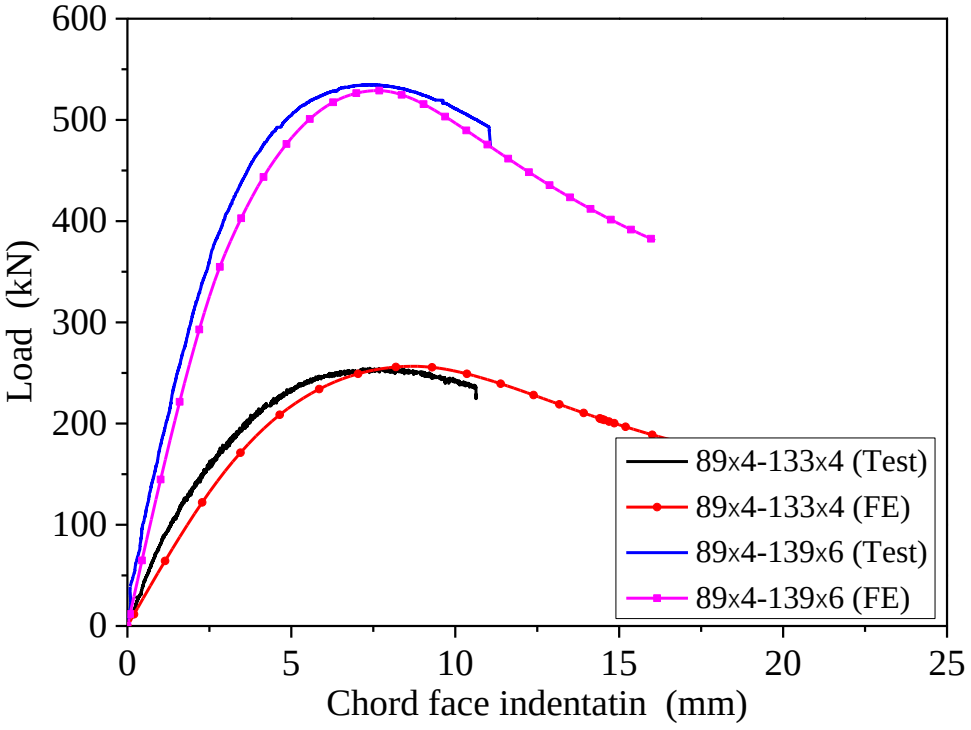

(b) Comparison of load-chord face indentation curves

Figure 11: Comparison of load-deformation curves between test and FE results

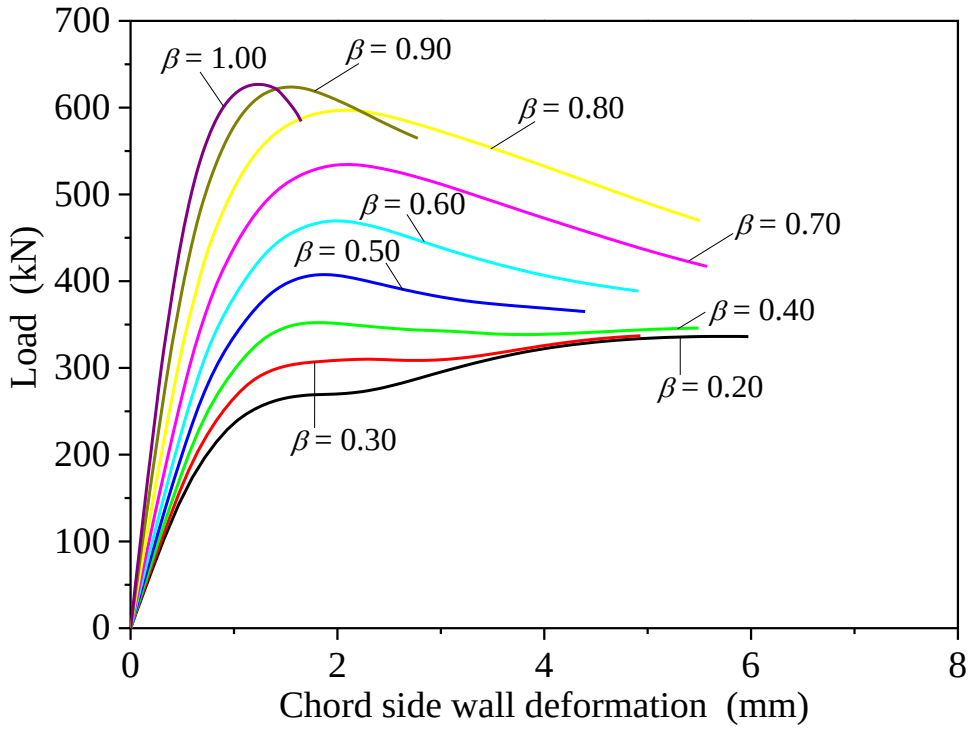

(a) Load-chord side wall deformation curves

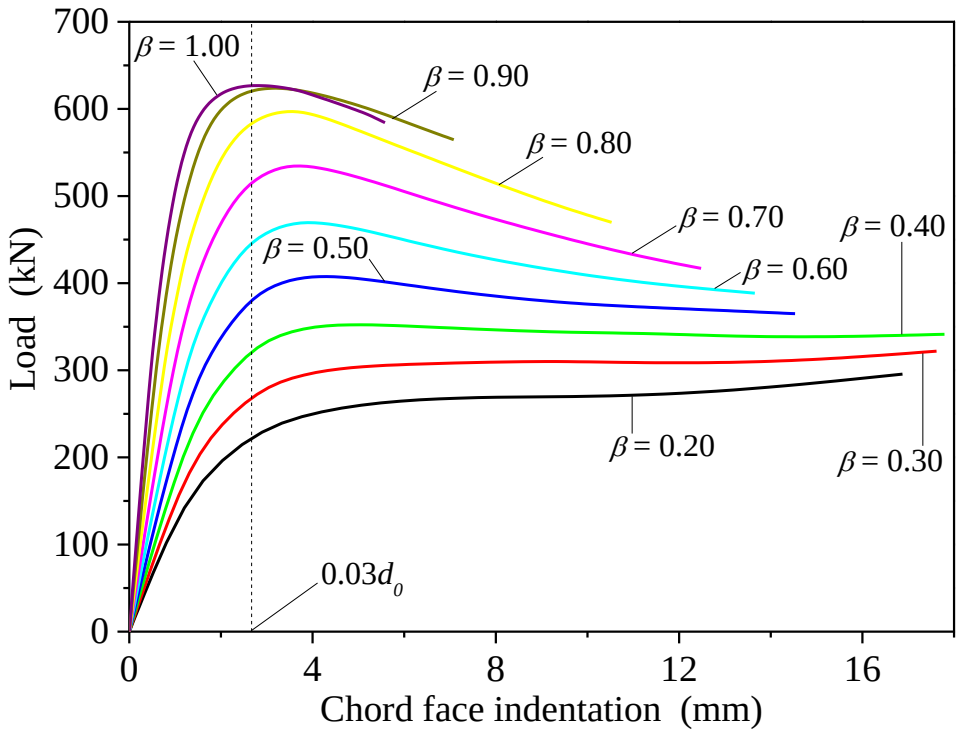

(b) Load-chord face indentation curves

Figure 12: Curves of Series A with $\tau = 1.00$ and $2\gamma = 14.11$

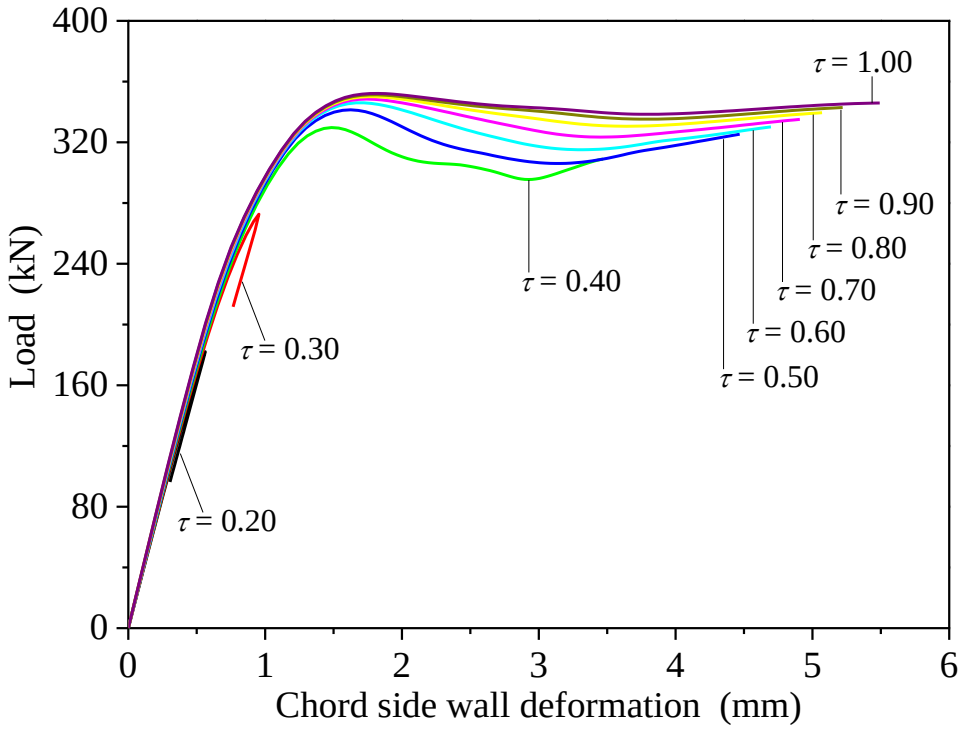

(a) Load-chord side wall deformation curves

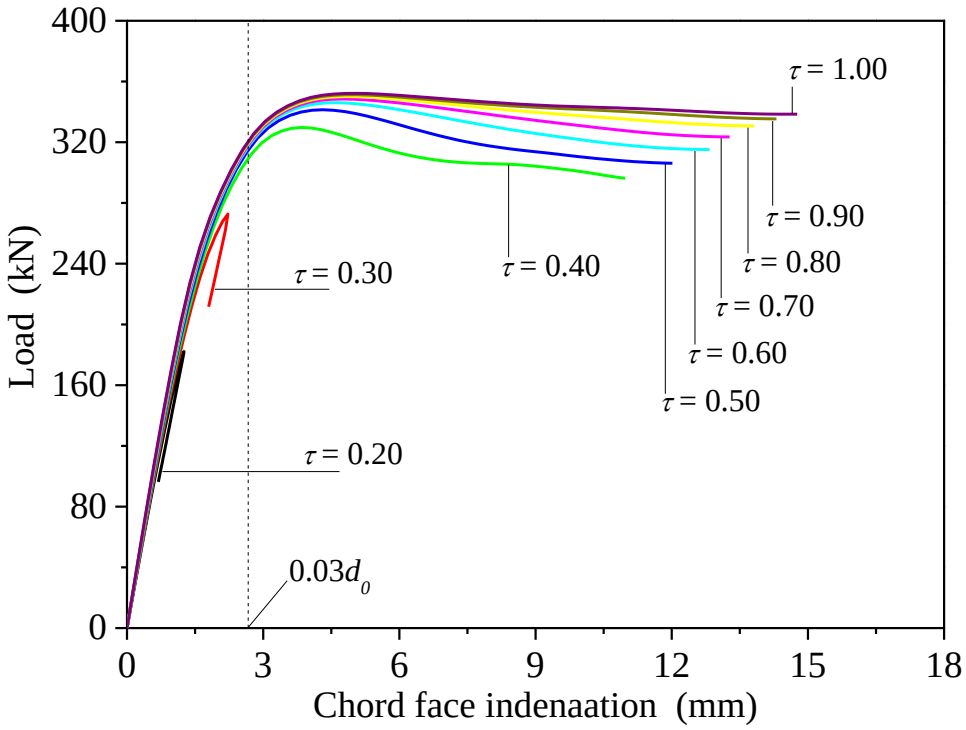

(b) Load-chord face indentation curves

Figure 13: Curves of Series A with β = 1.00 and 2γ = 14.11

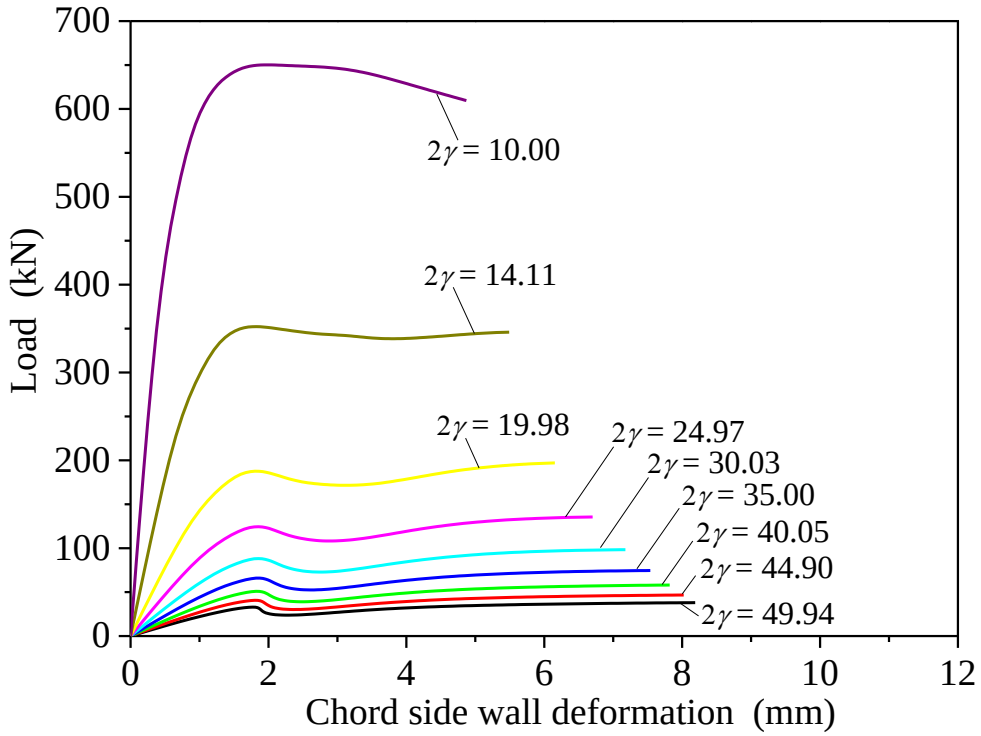

(a) Load-chord side wall deformation curves

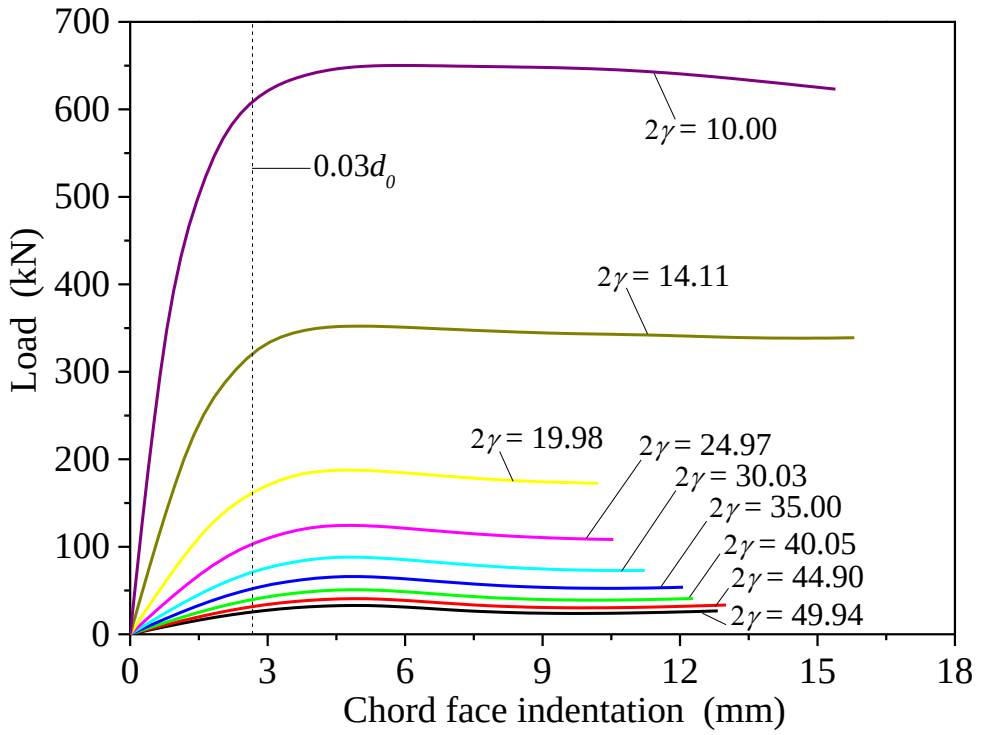

(b) Load-chord face indentation curves

Figure 14: Curves of Series A with β = 1.00 and τ = 1.00

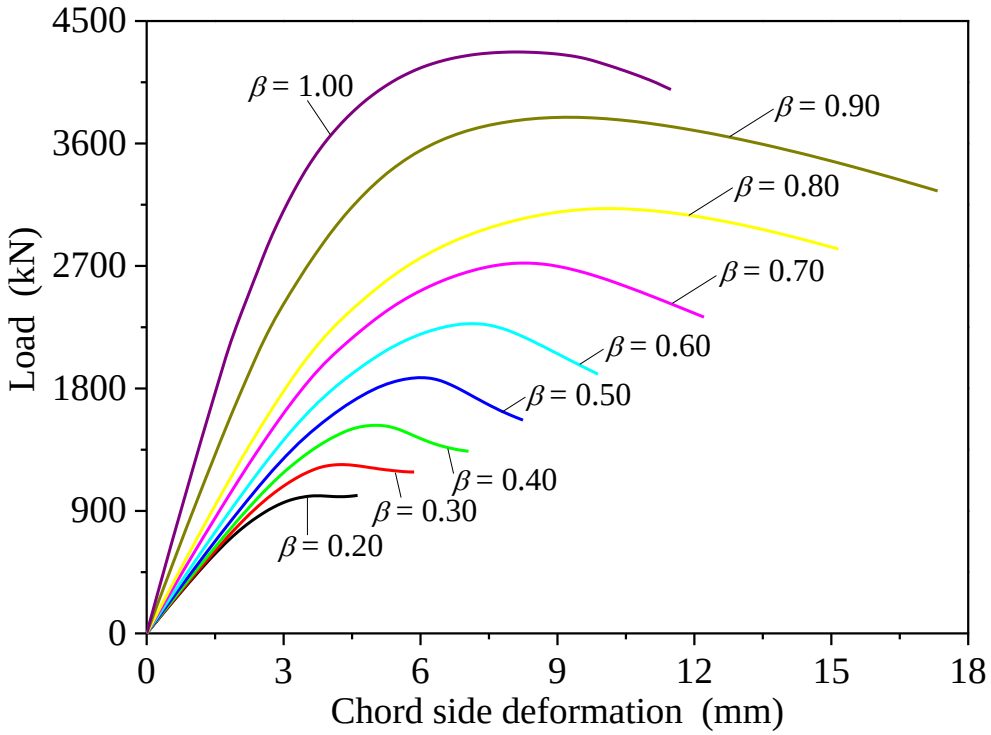

(a) Load-chord side wall deformation curves

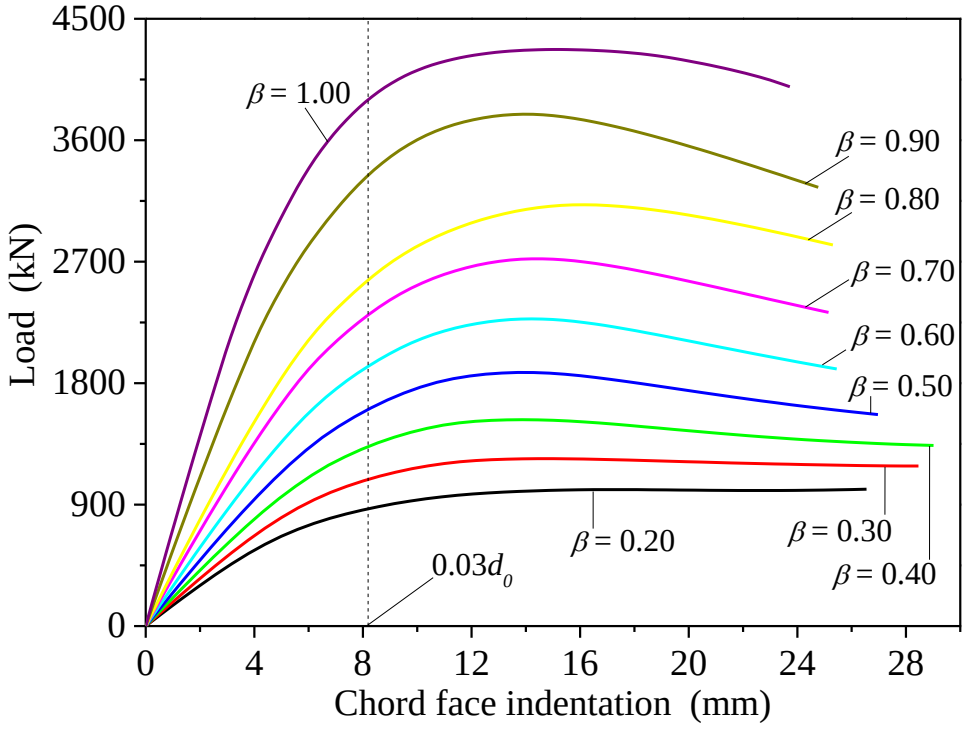

(b) Load-chord face indentation curves

Figure 15: Curves of Series B with $\tau = 0.60$ and $2\gamma = 21.84$

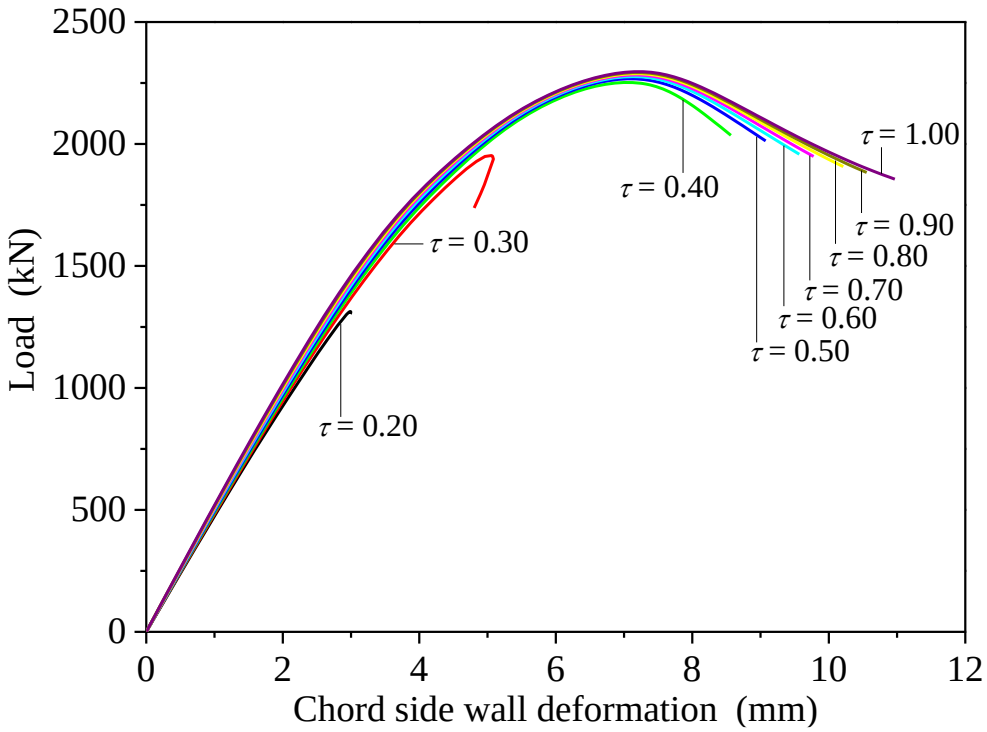

(a) Load-chord side wall deformation curves

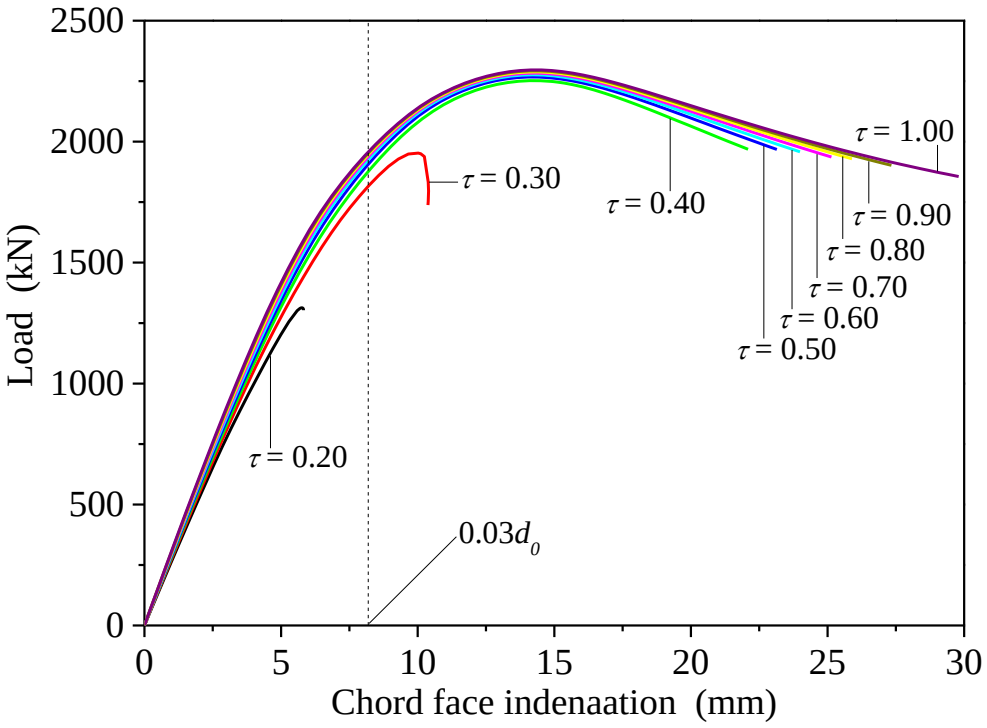

(b) Load-chord face indentation curves

Figure 16: Curves of Series B with β = 0.60 and 2γ = 21.84

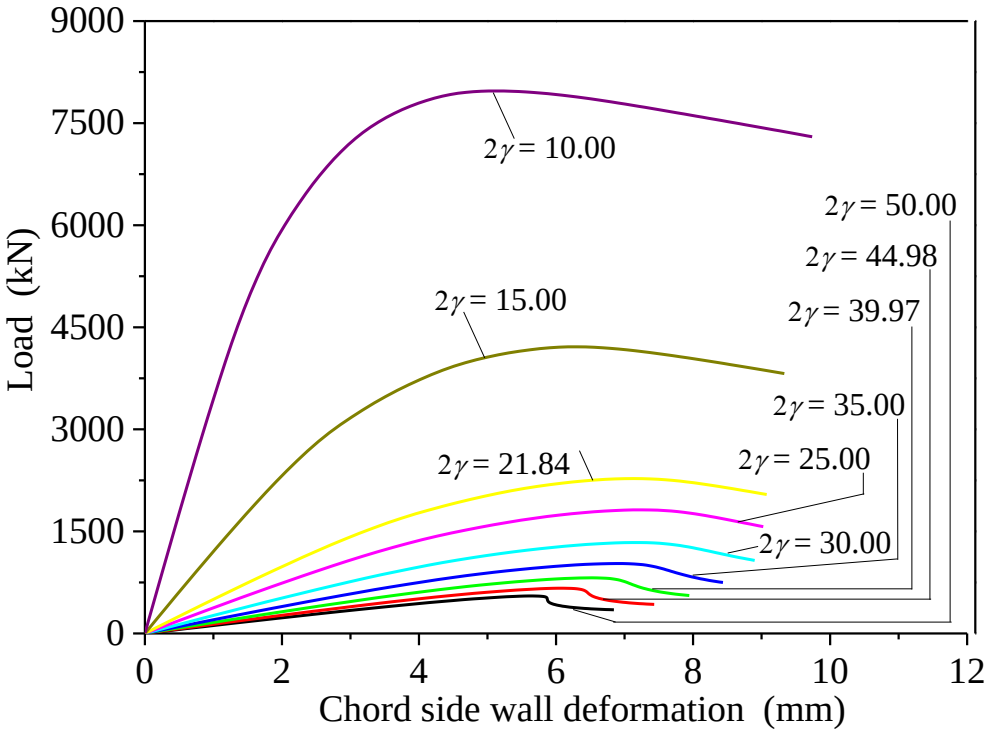

(a) Load-chord side wall deformation curves

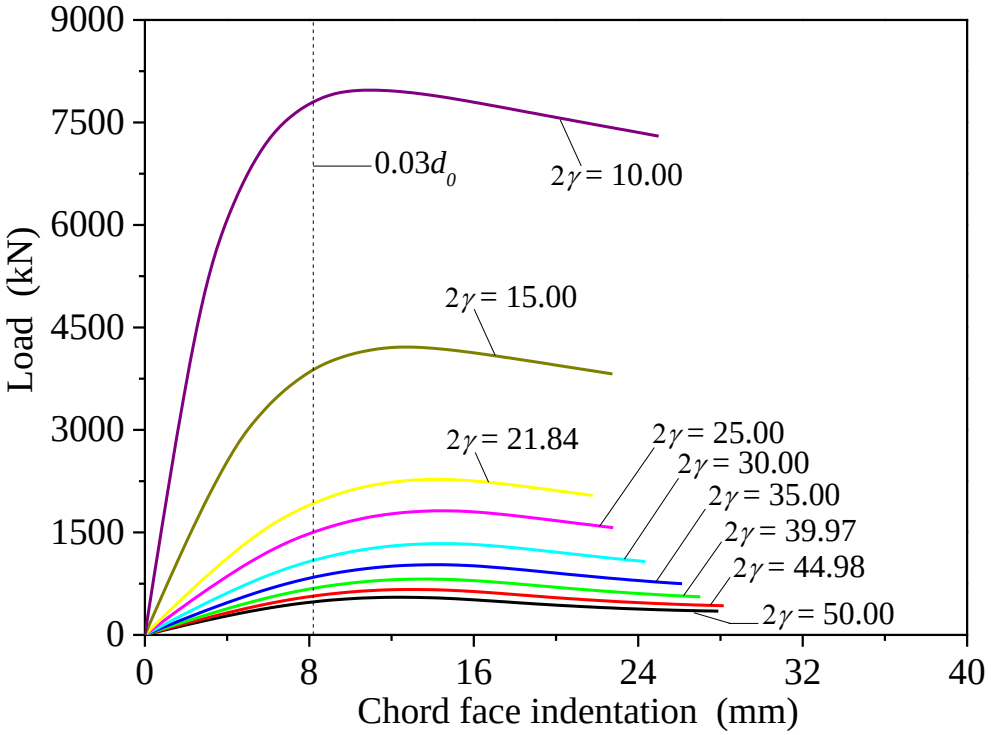

(b) Load-chord face indentation curves

Figure 17: Curves of Series B with β = 0.60 and τ = 0.60

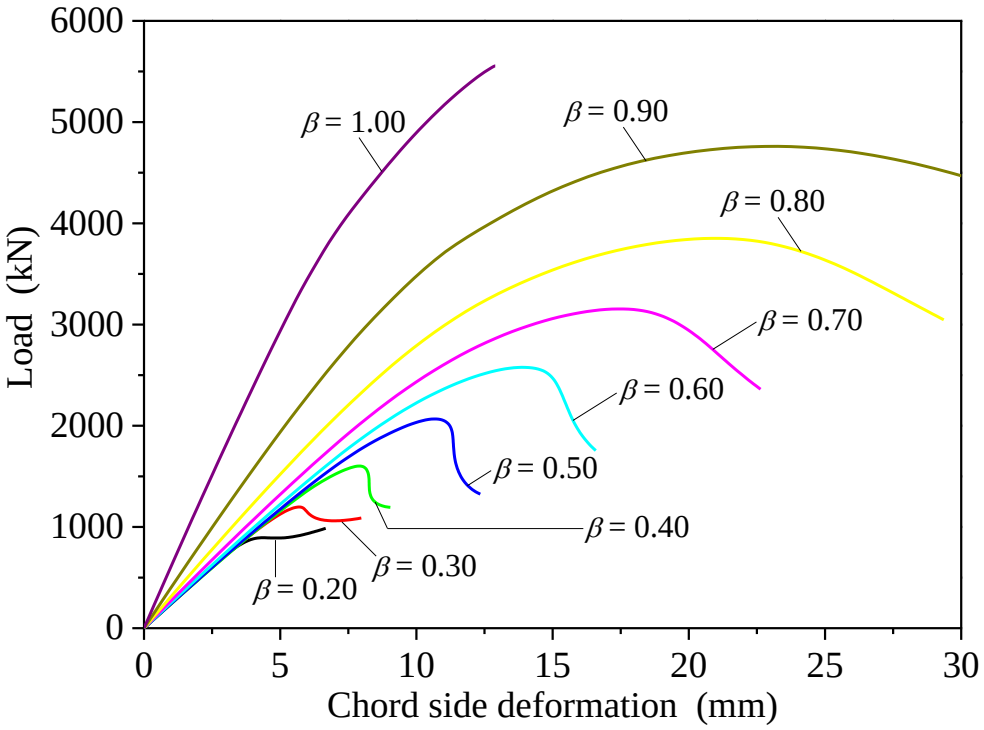

(a) Load-chord side wall deformation curves

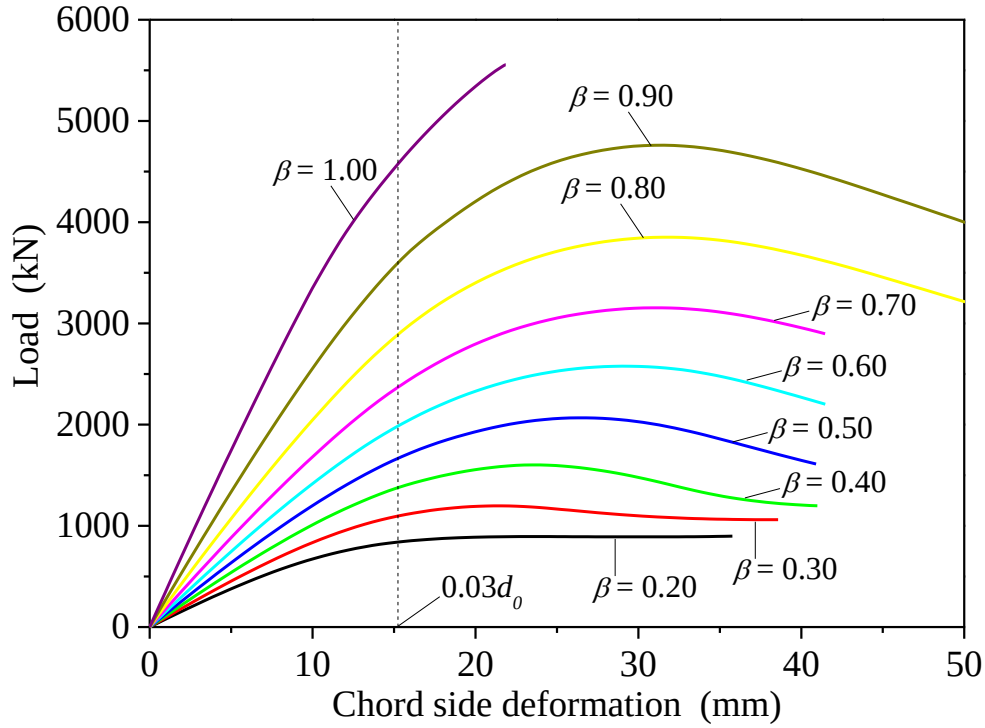

(b) Load-chord face indentation curves

Figure 18: Curves of Series C with $\tau = 0.40$ and $2\gamma = 40.64$

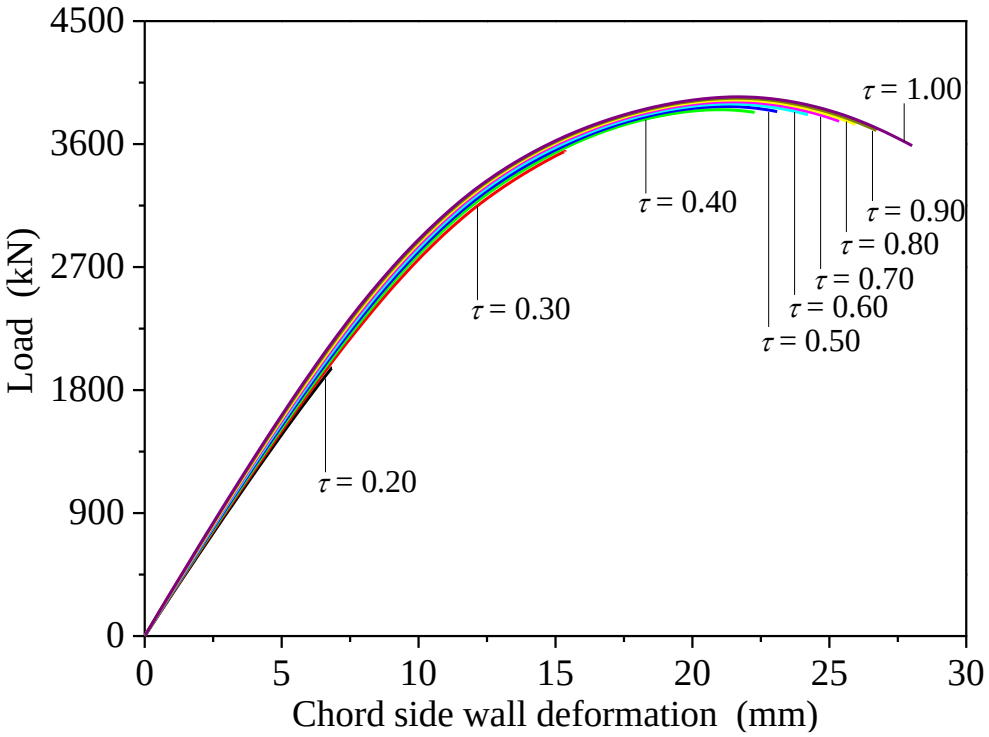

(a) Load-chord side wall deformation curves

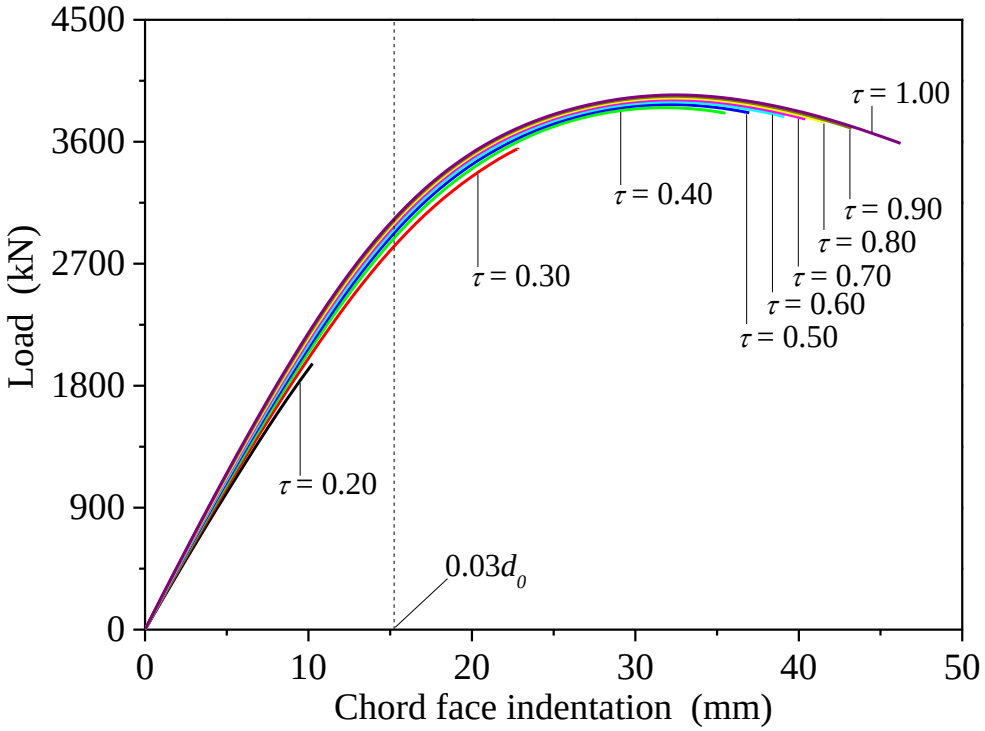

(b) Load-chord face indentation curves

Figure 19: Curves of Series C with β = 0.80 and 2γ = 40.64

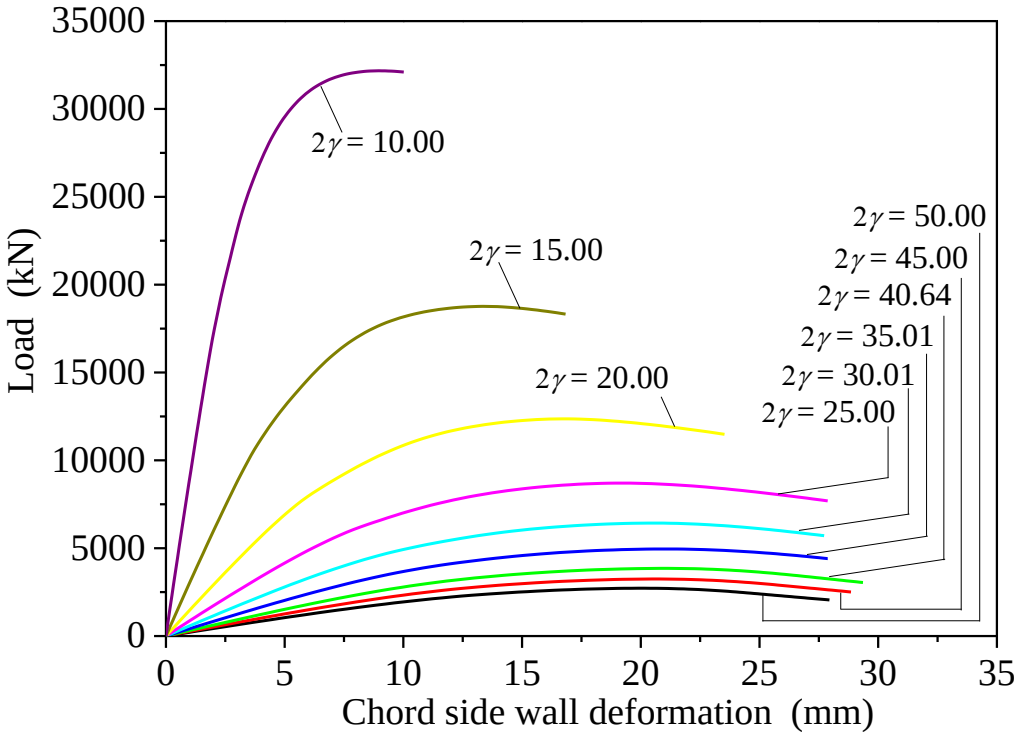

(a) Load-chord side wall deformation curves

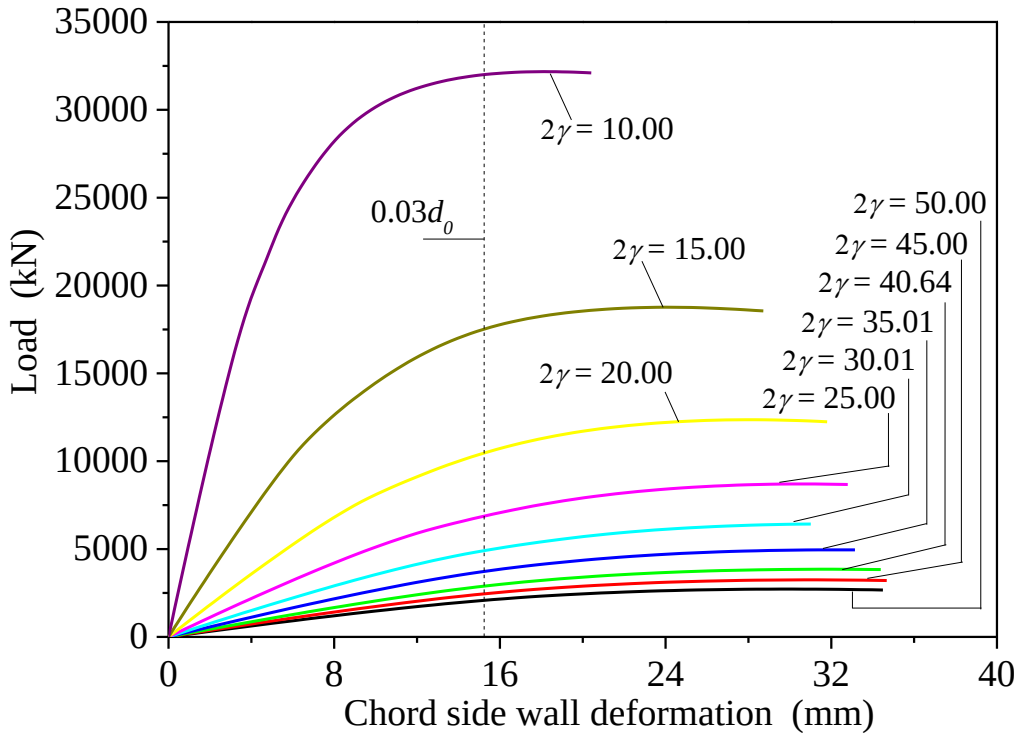

(b) Load-chord face indentation curves

Figure 20: Curves of Series C with β = 0.80 and τ = 0.40

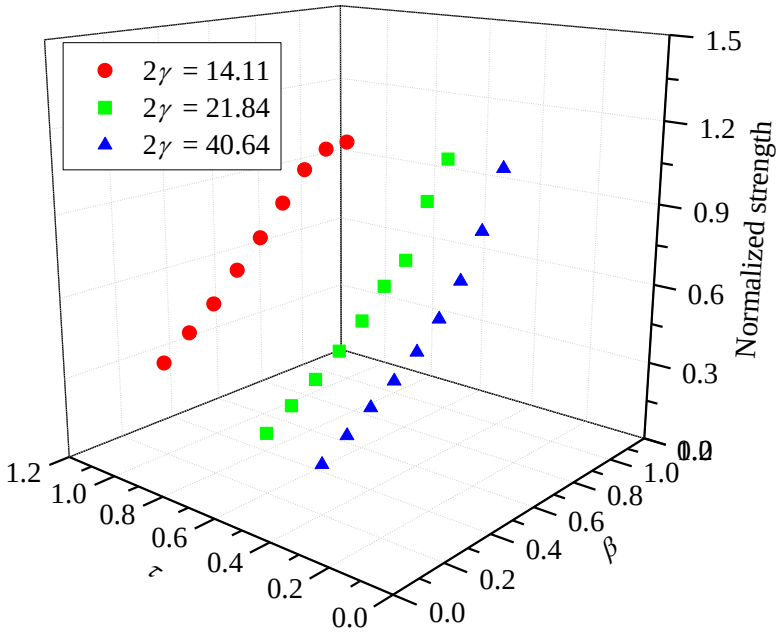

Figure 21: Effects of β on the CFHSS circular tubular T-joint strengths

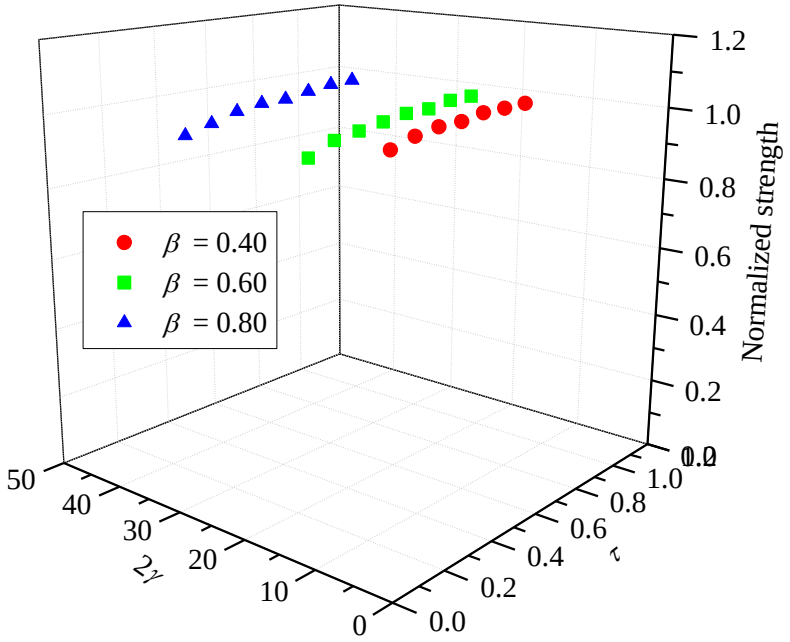

Figure 22: Effects of τ on the CFHSS circular tubular T-joint strengths

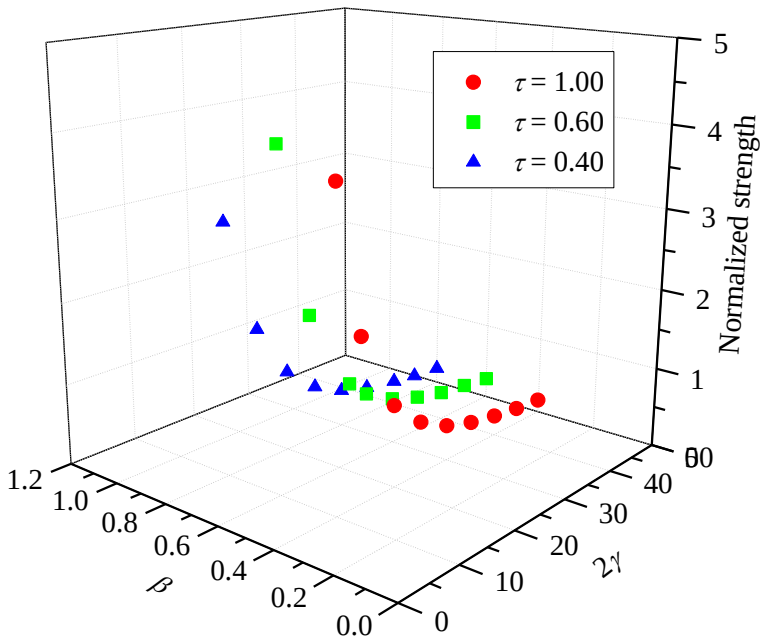

Figure 23: Effects of 2γ on the CFHSS circular tubular T-joint strengths

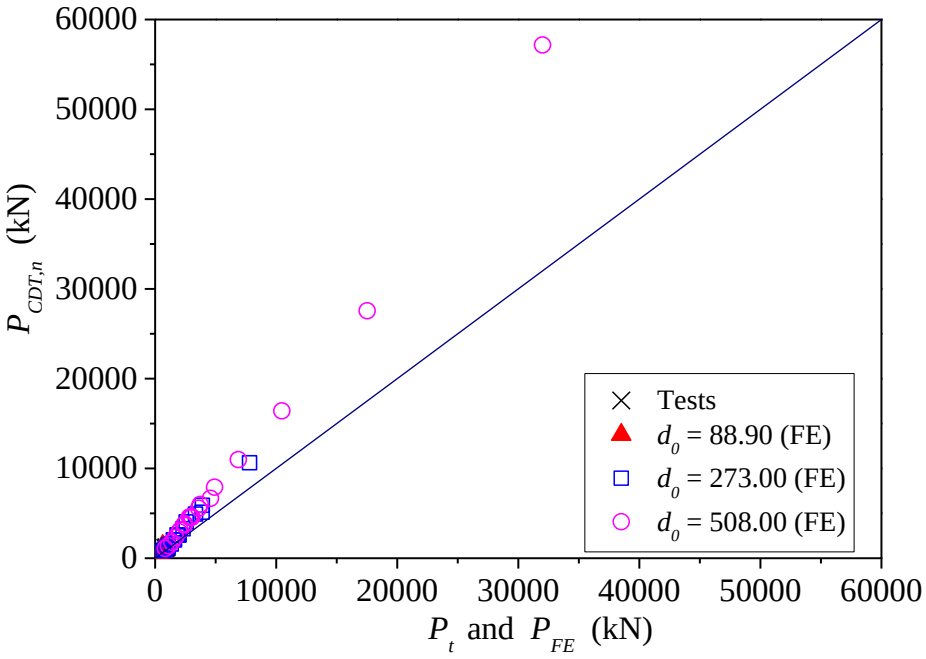

(a) Overall comparisons

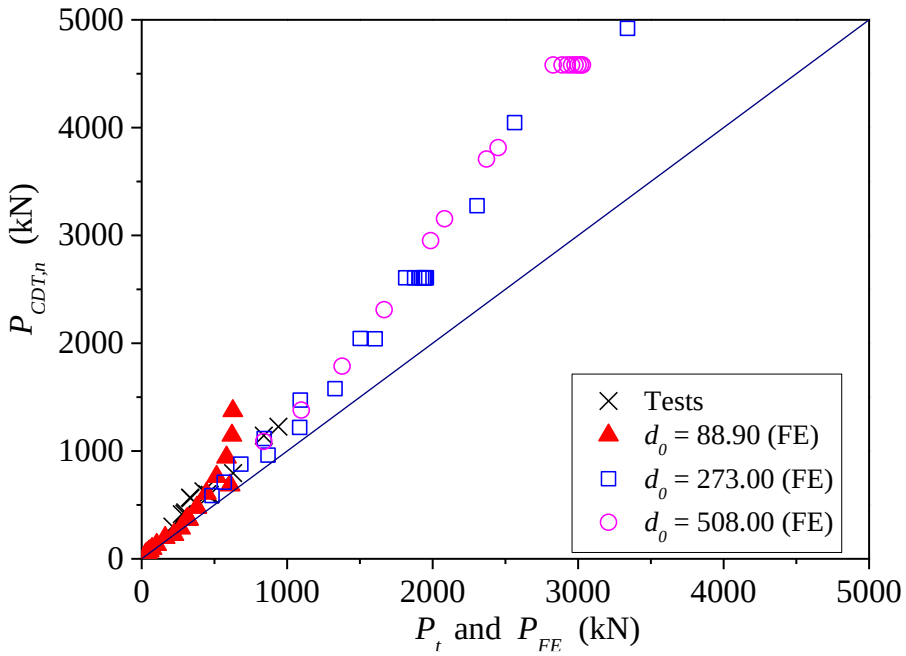

(b) Plot up to 5000 kN

Figure 24: Comparison of test and FE strengths with predictions by CIDECT [52]

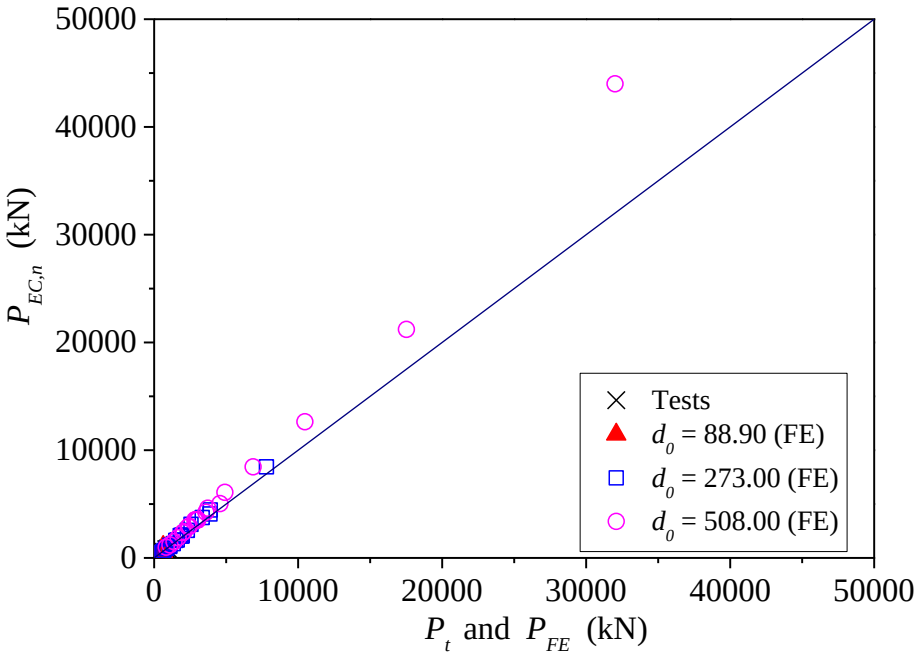

(a) Overall comparisons

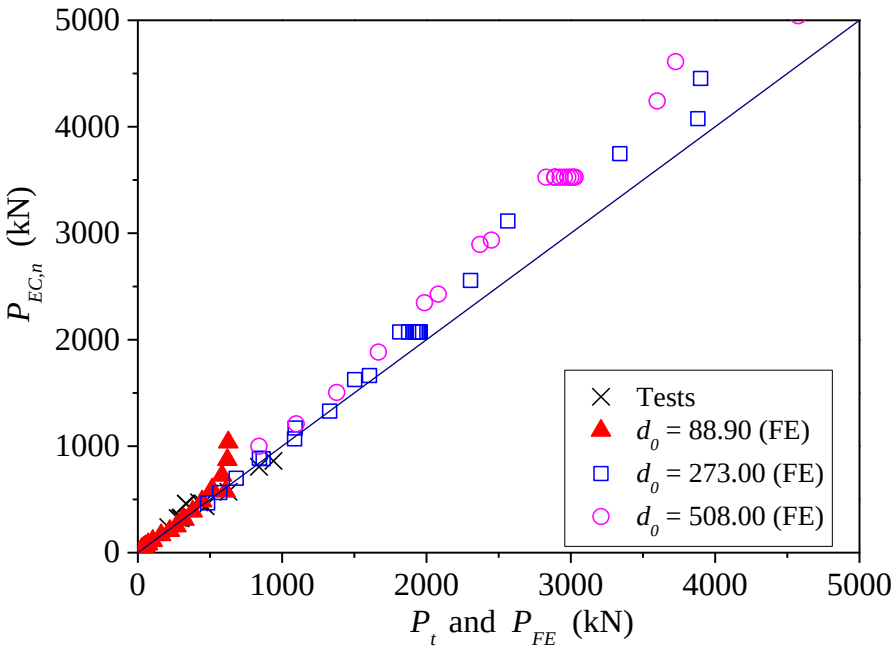

(b) Plot up to 5000 kN

Figure 25: Comparison of test and FE strengths with predictions by EN-1993-1-8 [55]

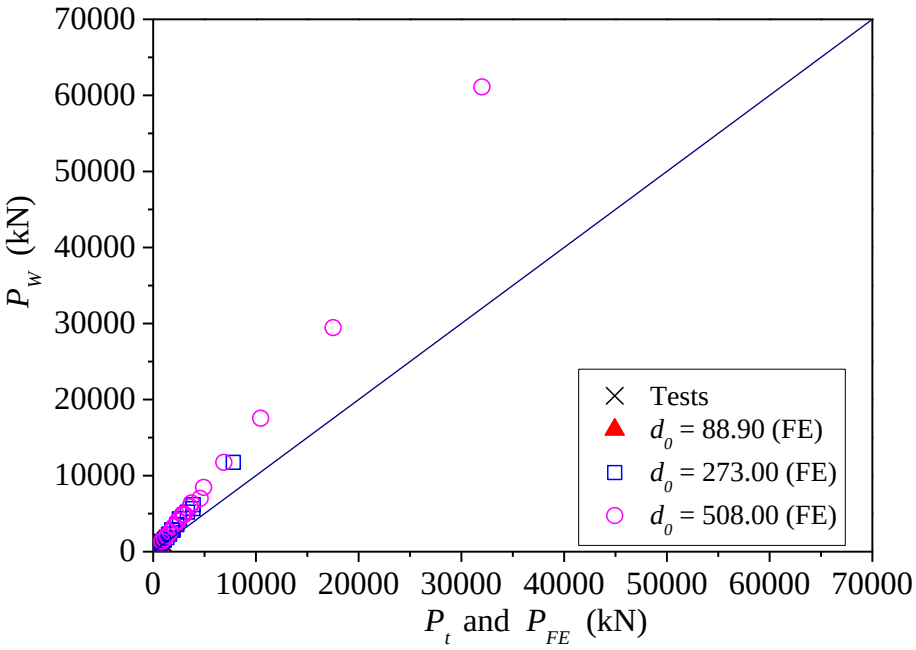

(a) Overall comparisons

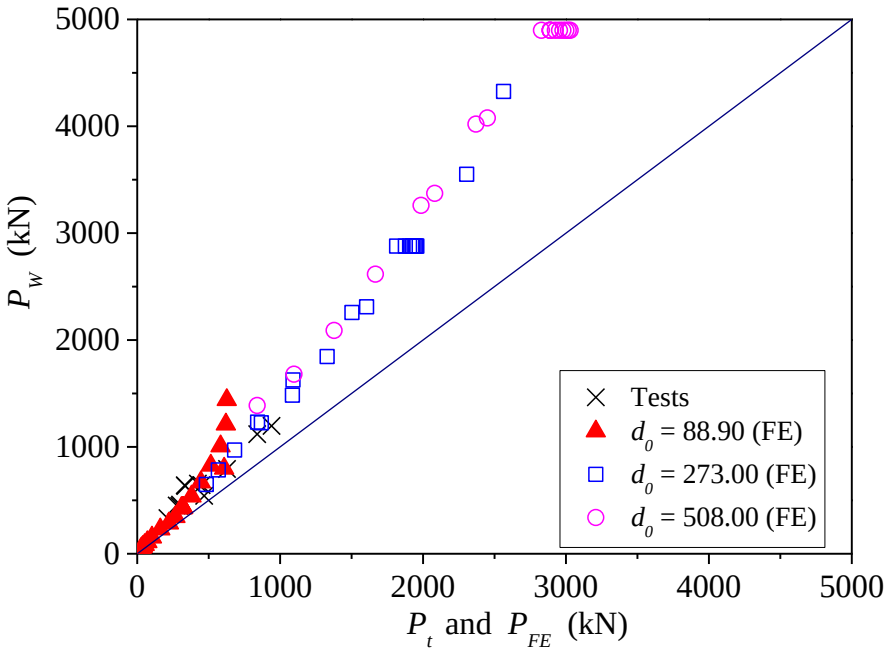

(b) Plot up to 5000 kN

Figure 26: Comparison of test and FE strengths with predictions by Wardenier [67]

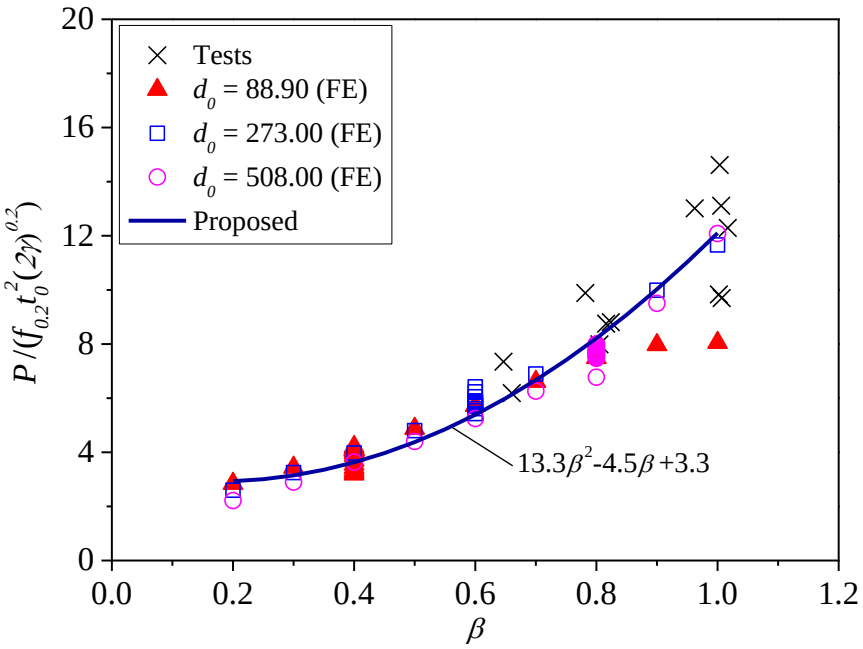

Figure 27: Relationship between joint strengths divided by $(f_{0.2}t_0^2(2\gamma)^{0.2})$ and β

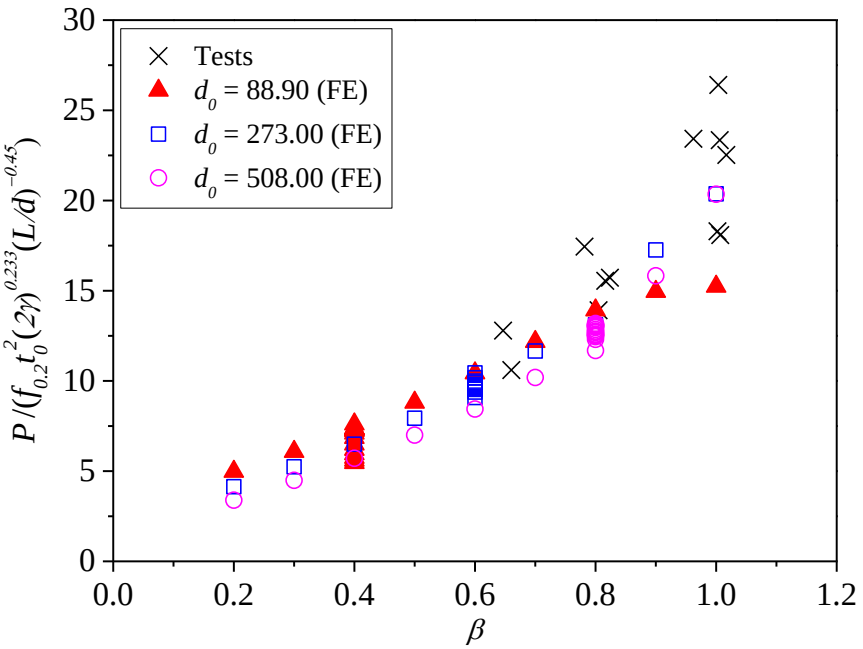

Figure 28: Relationship between joint strengths divided by $(f_{0.2}t_0^2(2\gamma)^{0.233}(L/d)^{-0.45})$ and β

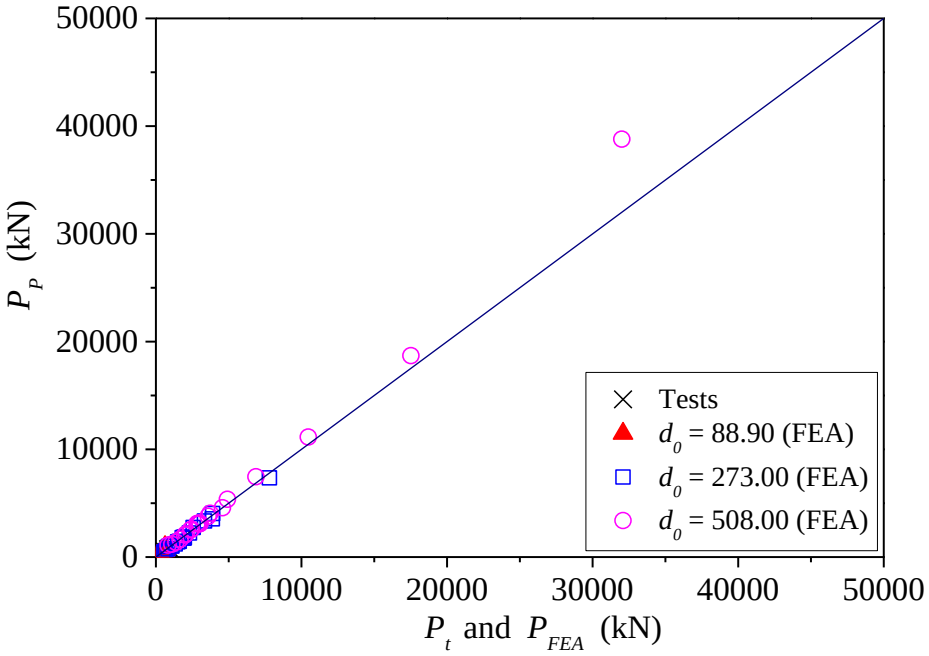

(a) Overall comparisons

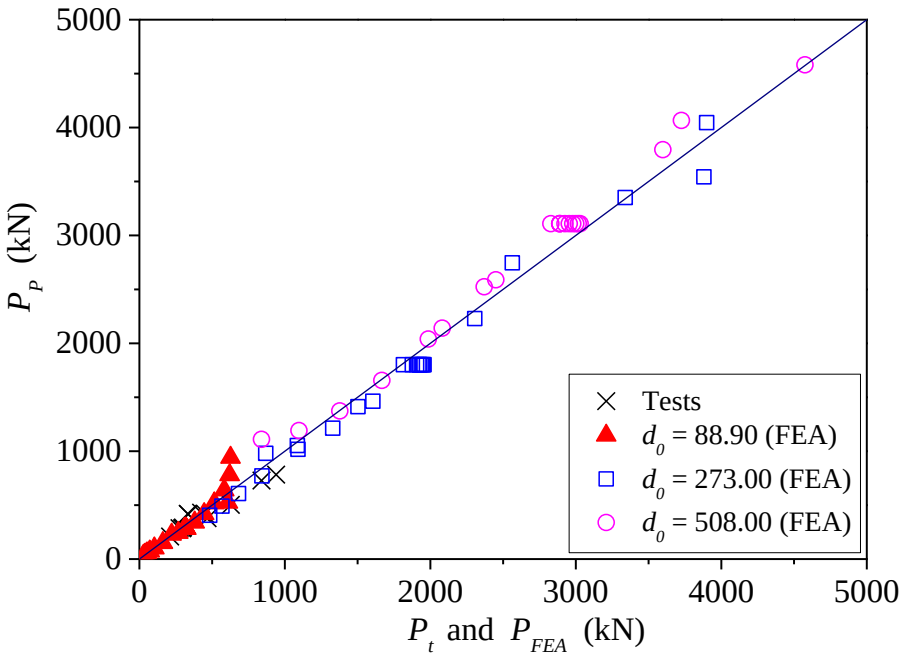

(b) Scale up to 5000 kN

Figure 29: Comparison of test and FE strengths with predictions by proposed equation